




Low-ionization structures in planetary nebulae - II. Densities, temperatures, abundances and excitation of 6 PNe

M. Belén Mari¹  , Denise R. Gonçalves¹ and Stavros Akras² 

¹Observatório do Valongo, Universidade Federal do Rio de Janeiro, Ladeira Pedro Antonio 43, Rio de Janeiro 20080-090, Brazil

²Institute for Astronomy, Astrophysics, Space Applications and Remote Sensing, National Observatory of Athens, Penteli GR 15236, Greece

Accepted XXX. Received YYY; in original form ZZZ

ABSTRACT

Here we present the spatially resolved study of six Galactic planetary nebulae (PNe), namely IC 4593, Hen 2-186, Hen 2-429, NGC 3918, NGC 6543 and NGC 6905, from intermediate-resolution spectra of the 2.5 m Isaac Newton Telescope and the 1.54 m Danish telescope. The physical conditions (electron densities, N_e , and temperatures, T_e), chemical compositions and dominant excitation mechanisms for the different regions of these objects are derived, in an attempt to go deeper on the knowledge of the low-ionization structures (LISs) hosted by these PNe. We reinforce the previous conclusions that LISs are characterized by lower (or at most equal) N_e than their associated rims and shells. As for the T_e , we point out a *possible* different trend between the N and O diagnostics. $T_e[\text{N II}]$ does not show significant variations throughout the nebular components, whereas $T_e[\text{O III}]$ appears to be slightly higher for LISs. The much larger uncertainties associated with the $T_e[\text{O III}]$ of LISs do not allow robust conclusions. Moreover, the chemical abundances show no variation from one to another PN components, not even contrasting LISs with rims and shells, as also found in a number of other works. By discussing the ionization photon flux due to shocks and stellar radiation, we explore the possible mechanisms responsible for the excitation of LISs. We argue that the presence of shocks in LISs is not negligible, although there is a strong dependence on the orientation of the host PNe and LISs.

Key words: ISM: kinematics and dynamics – ISM: abundances – ISM: jets and outflows – planetary nebulae: individual: IC 4593, Hen 2-186, Hen 2-429, NGC 3918, NGC 6543, NGC 6905.

1 INTRODUCTION

Planetary nebulae (PNe) represent the final stages on the evolution of low- and intermediate-mass stars. They are formed after the ejection of their outer envelopes, from the multiple stellar wind episodes occurred in the previous evolutionary stages and resulting in a complex bulk of ionized matter. Besides the large-scale components of PNe, such as shells, rims or halos, identified mainly from the emission of bright forbidden [O III] together with H recombination lines, much smaller components are also recognized in PNe, due to their enhanced emission from low-ionization species, such as [N II], [O II], [S II] or [O I] (see e.g. Corradi et al. 1996; Balick et al. 1998; Gonçalves et al. 2001; Akras & Gonçalves 2016, hereafter Paper I). These macro- and micro-structures are clearly recognizable in PNe’ imaging catalogs such as Balick (1987), Schwarz et al. (1992), Machado et al. (1996), Corradi et al. (1996) or Górny et al. (1999).

Gonçalves et al. (2001) compiled and classified these structures – in terms of their morphology and kinematics – as knots, filaments, jets and jet-like systems, which show up in axisymmetric pairs or isolated. To account for such variety of features, specific nomenclatures also appear in the literature (Balick et al. 1993; Lopez et al. 1995; Perinotto 2000). Moreover, in the above quoted compilation the morphological and kinematic properties of low-ionization structures (LISs) of the 50

PNe sample were also compared with the predictions from theoretical models. The main conclusions then guided other studies with the aim of better constrain LISs’ formation models. However, the enhanced low-ionization emission lines of LISs, relative to their surrounding medium, is still a perplexing issue, although observational evidence for their association with a not-insignificant molecular counterpart is becoming more and more appealing (Reay et al. 1988). For recent ideas on the relation between the intensity of low-ionization emission lines and the H₂ content of PNe, focusing the small-scale structures, see e.g. Gonçalves et al. (2009); Machado et al. (2015); Ramos-Larios et al. (2017); Akras et al. (2017, 2020b).

Several observational works, sometimes with tailored models to explain the observations, have been conducted to characterise LISs’ physical and chemical properties (e.g. Balick et al. 1993, 1994, 1998; Hajian et al. 1997; Gonçalves et al. 2003, 2004, 2006, 2009; Akras & Gonçalves 2016; Danehkar et al. 2016; Ali & Dopita 2017; Monreal-Ibero & Walsh 2020; Miranda et al. 2021). The overall conclusions derived thus far are: (i) LISs occur in PNe of all different morphological types; (ii) LISs’ electron temperatures are similar to those of the main nebular components; (iii) the electron densities of the main structures are higher than or equal to those measured for LISs; and (vi) there is no chemical abundance enrichment in LISs, i.e., all the nebular components have similar chemical composition.

Even though, the LISs’ kinematics were studied in detail for a number of PNe (for instance in Steffen et al. 2001; García-Díaz

* E-mail: mbmari@astro.ufrj.br

et al. 2012; Corradi et al. 1999, 2000a,b; Akras & López 2012; Derlopa et al. 2019), a general knowledge about the kinematics of the LISs was missing until recently, when, at least for the case of pairs of jets/knots, this issue was solved. From a sample of 85 jets hosted by 58 PNe, Guerrero et al. (2020b) found that jets can be divided into two populations: (i) those with spatial velocities below 100 km s^{-1} , which represent $\sim 70\%$ of the sample, and (ii) those with mean velocities near 180 km s^{-1} . Comparing the observed spatial and velocity distribution of jets, authors concluded that jets are mainly coeval with their parent PNe.

Regarding the knots, it is necessary to consider whether they occur in pairs or isolated, since it is counter-intuitive to necessarily link the formation of both kinds to the same physical processes. For the latter, Matsuura et al. (2009) convincingly showed that the isolated knots are part of the nebula's inner ring being swept by the faster stellar wind. Similar conclusions were reached by Machado et al. (2015) by studying the molecular waist of NGC 2346. These two results are not in conflict with the argument that isolated knots (or part of them) originate *in situ* from the neutral AGB wind and are subsequently excited by shocks (e.g. García-Segura et al. 2006) or by the central star radiation field (Dyson et al. 1989; Soker 1998).

For the case of the pairs of knots, whilst a consensus has not yet been reached, the most promising recent models of magneto- or purely-hydrodynamic jet launching are converging to binaries with magnetic fields as the minimum requirement for the formation of collimated outflows. This is particularly true to account for highly collimated pairs of jets and knots. A number of works explore these arguments, and we refer the readers to Gonçalves et al. (2001); Balick & Frank (2002); Guerrero et al. (2020b) works, on which the theoretical efforts are reviewed, almost 2 decades apart. Moreover, the state of the art of such models (simulations) can be found in the following latest contributions: García-Segura et al. (2018, 2020, 2021) as well as Balick et al. (2019, 2020). Also to be mentioned is the series of studies starting with Akashi & Soker (2008), that simulate light-jets – whose density are much lower than the density of the slow wind – which end up producing collimated PN shells and dense pairs of knots.

Explicitly meant to form jets/pairs of knots, Balick et al. (2020) had convincingly shown, via magneto-hydrodynamic simulations, that very dense axial knots formed in the slow, heavy flows that account for collimated pre-PNe and mature PNe eventually become the observed low-ionization knots, once their surfaces start to become ionized. This simulation predicts that these LISs' high densities (10^{5-7} cm^{-3} ; their Fig. 6) and related UV opacities assure that LISs' interiors remain neutral and cold ($3 \times 10^{0-2} \text{ K}$; their Fig. 6); and with kinematics compatible with Guerrero et al. (2020b) compilation. Such high densities in LISs have also been suggested for providing the necessary condition to self-shield the molecular hydrogen (H_2) recently discovered in some LISs from the stellar far-UV radiation (Marquez-Lugo et al. 2013; Machado et al. 2015; Fang et al. 2015, 2018; Akras et al. 2017, 2020b).

In this paper, we present the analysis of spectroscopic data of a sample of 6 PNe with LISs, in order to obtain the spatial physico-chemical properties together with the excitation mechanisms present in these intriguing structures and their surrounding nebulae. The observations and the procedure to analyse the data are described in section 2 and 3, respectively. In section 4 we present the results of spectroscopic analysis of the different structural components for the six PNe. Finally, in sections 5 and 6, we present the discussions and conclusions.

Table 1. Log of observations obtained with INT telescope in 2001 (1) and the Danish telescope in 1997 (2).

PN name	Date	PA	Exposure [s]	Seeing [†]	Airmass
IC 4593 ⁽¹⁾	08-29	62°	120, 300, 1200	1.1-1.2	1.21
	08-29	139°	120, 300, 1200	1.0-1.2	1.66
Hen 2-186 ⁽²⁾	04-11	29°	60, 300, 1800	2.1	1.11
Hen 2-429 ⁽¹⁾	08-29	89°	1800	1.8	1.44
	04-11	30°	60,300	1.6	1.14
	04-11	40°	300	1.7	1.17
	04-10	42°	1800	1.7	1.18
NGC 3918 ⁽²⁾	04-10	70°	20, 300	1.7	1.39
	04-10	70°	20, 300	1.7	1.39
NGC 6543 ⁽¹⁾	08-28	5°	20, 300	1.3-1.4	1.27
	09-04	163°	300, 1200	1.2-1.3	1.43
NGC 6905 ⁽¹⁾	08-31	161°	300, 2700	1.4	1.17

Note: [†]Obtained through the FWHM of the stellar continuum measured in the spectra.

2 OBSERVATIONS

Low-resolution spectra of six PNe with embedded LISs were obtained using the 2.5 m Isaac Newton Telescope (INT) at the Observatorio Roque de los Muchachos, Spain, and the 1.54 m Danish telescope at the European Southern Observatory (ESO) at La Silla, Chile. INT and Danish data were taken, respectively, in August and September of 2001, and April 1997.

The Intermediate Dispersion Spectrograph (IDS) mounted on the INT was used in conjunction with the 235 mm camera providing a spatial scale of $0.70 \text{ arcsec pixel}^{-1}$ with the TEK5 CCD and the R300V grating, thus providing a spectral resolution of $3.3 \text{ \AA pixel}^{-1}$ and a wavelength covering of $3650\text{--}7000 \text{ \AA}$. The slit width and length were 1.5 arcsec and 4 arcmin , respectively.

The Danish Faint Object Spectrograph mounted in the Danish telescope was used in conjunction with the DFOSC $2000 \times 2000 \text{ CDD}$ camera, resulting in a spatial scale of $0.40 \text{ arcsec pixel}^{-1}$, and the Grism#4 ($300 \text{ lines mm}^{-1}$), which results in a wavelength range of $3600\text{--}8000 \text{ \AA}$ and spectral resolution of $2.2 \text{ \AA pixel}^{-1}$. The slit width was 1.0 arcsec and the slit length was $> 13.7 \text{ arcmin}$.

Several spectra have been obtained per PN, in different position angles (PA) and/or different exposure times (in order to avoid possible saturation of the usually brightest emission lines; e.g. [O III], H α). The log of the observations is listed in Table 1. The reduction/analysis of the data was made using the LONGSLIT package in IRAF following the standard procedure: bias subtraction, flat-field correction and wavelength calibration using lamp frames. For the flux calibration of the spectra, spectro-photometric standard stars were observed and the flux calibration was also made with IRAF.

Observations were carried out taking into account the parallactic angle in order to avoid the differential chromatic refraction (DCR) effect, which mainly affects the blue side of the spectrum (see e.g., Montoro-Molina et al. 2022). However, in some cases the PA used did not coincide with the parallactic angle and the DCR effect on these spectra was estimated. Taking into account the airmass (or $\sec(z)$), altitudes of $\sim 2 \text{ km}$, and latitudes of $\sim \pm 30^\circ$ per telescope, the DCR were derived from the equations of Filippenko (1982). Considering the bluest ([O II] $\lambda 3727$) and reddest ([S II] $\lambda 6731$) lines of interest, we observe that the DCR effect could be present only in two cases. In IC 4593 (PA=139°) and in NGC 3918 (PA=70°), which amount at most to $\sim 1.9 \text{ arcsec}$ and $\sim 1.4 \text{ arcsec}$, respectively. Nevertheless,

comparing the results obtained for different PA and structures of these nebulae (see Tables A1 and A7), we observe that DCR does not substantially affect the measurements on which we based our conclusions in this work.

3 NEBULAR DIAGNOSTICS

First, the emission line fluxes were computed considering a Gaussian distribution in IRAF. Then, the Nebular Empirical Analysis Tool (NEAT, Wesson et al. 2012) was employed for the analysis. NEAT was used to identify the lines, compute the extinction coefficient (c_β), electron densities (N_e) and temperatures (T_e) as well as ionic (X^+/H^+) and total abundances (X/H). NEAT uses the flux-weighted ratios of $H\alpha$, $H\gamma$ and $H\delta$ to $H\beta$ to calculate and correct the line fluxes for the interstellar extinction adopting the Galactic reddening law of Howarth (1983), with $R_V = A_V/E(B - V) = 3.1$.

The emission line intensities, in units of $H\beta=100$, together with c_β , N_e and T_e are listed in odd tables (A1-A11) for several nebular components extracted from specific windows that are illustrated in Figures 1 to 7. Electron temperatures and densities were computed for different diagnostic lines. For the particular case of N_e estimation using the [Ar IV] diagnostic lines, the theoretical value of $He\ I\ 4713/4471=0.146$ (Benjamin et al. 1999) was used (considering $T_e=10^4$ K and $N_e=10^4\text{ cm}^{-3}$) to correct the blended [Ar IV] $\lambda 4711+He\ I\ \lambda 4713$ emission from the contribution of the He recombination line.

For the ionic and total abundance calculations, as discussed by Wesson et al. (2012), the temperatures and densities that are more appropriate for the ionization potentials of the ionized gas are used. To correct for the unobserved ions, the ionization correction factors (ICF) of Delgado-Inglada et al. (2014) were adopted, except for Ar/H and S/H, in which the ICFs from Kingsburgh & Barlow (1994) were used. The ionic and total abundances, per PN nebular components, are listed in even tables (A2-A12). For the Ne^{2+}/H^+ derived from the [Ne III] $\lambda 3967$ line, we applied the correction for the contribution of the $He\ \lambda 3970$ line, considering the theoretical ratio $He/H\beta \sim 0.158$ (Osterbrock & Ferland 2006).

It should be noted that NEAT uses a Monte Carlo scheme to calculate the statistical uncertainties of the parameters, based on the flux uncertainties and their propagation through the diagnostics¹. Errors related with N_e and T_e were obtained directly from the uncertainties of the lines involved on the diagnostic ratio, as in the previous papers of the series (Gonçalves et al. 2003, 2004, 2009; Akras & Gonçalves 2016; Mari et al. 2020).

4 RESULTS

In the next subsections we present the spectroscopic analysis of six PNe, for the different morphological structures – LISs, shells, rims and a portion of the nebula along the various slit positions, generally of high-ionization, labeled as Neb. We also summarize the main results from the literature.

Figures 1 to 4, 6 and 7 show the above defined components, per nebula. The normalized flux distribution of the [N II] $\lambda 6584$ (solid-line) and [O III] $\lambda 5007$ (dashed-line) along the slits, as well as the ratio of these emission lines, are presented in the middle and lower panels of the figures. The line-ratio plots are extremely useful to define the

the regions of the spectra to extract the regions under analysis. Ideally, the underlying nebular emission should be subtracted from the LISs emission lines, to insure that LISs' properties are not contaminated by those of the large-scale nebular structures. However, with the current data, this is a cumbersome task. This kind of correction can be better addressed with IFU data, by computing the large-scale nebula structures emission from the surrounding region. A good example of such correction is by Montoro-Molina et al. (2022) who managed to resolve the inner region from the surrounding nebular emission in the velocity space. Therefore, we compute the emission lines from different nebular structures such as Neb, LISs and rims/shells, and compare the outcomes among these structures.

For the six PNe, the emission line fluxes, absolute flux of $H\beta$ (observed), c_β , N_e and T_e are presented in the odd tables (from Table A1 to A11). On the other hand, the ionic and total abundances of the nebular components are show on the even tables (from Table A2 to A12). The literature with which we compared the results of our diagnostics are listed in the captions of Figures 8 and 9.

4.1 IC 4593

In the optical, IC 4593 is a complex multiple-shell PN, with a roundish bright filamentary outer shell, with $\sim 16''$ in extension. The $(H\alpha+[N\ II])/[O\ III]$ ratio images from Corradi et al. (1996) revealed the presence of a pair of knots, which authors called jet-like features, located near $\sim 12''$ from the center and oriented along $PA=139^\circ$, as well as an isolated knot embedded in the inner layers along $PA=62^\circ$ (Fig. 1). According to Corradi et al. (1997) the jet-like features have radial velocities of 2 km s^{-1} , whereas for the isolated knot this value is of 1 km s^{-1} .

For the analysis of this nebula we selected the slit which contains the pair of LISs ($PA=139^\circ$) and the isolated one ($PA=62^\circ$), together with the inner shell (4 regions) and Neb. We, previously, studied this nebula and the results were presented in Mari et al. (2020), however, the emission-line fluxes were remeasured in an attempt to reduce uncertainties. The improved results are presented here.

The interstellar extinction coefficient of IC 4593 varies significantly between the components and slit positions, from 0.02 to 0.22, with an average value of 0.11 ± 0.02 . Interestingly, a similar wide range of c_β is found in the literature, from 0.01 (Costa et al. 1996, along E-W direction), 0.05 (Tylenda et al. 1992), 0.125 (Barker 1978a), 0.17 (Robertson-Tessi & Garnett 2005, along E-W direction) up to 0.24 ± 0.16 (Delgado Inglada et al. 2009, $PA=0$). This wide range of c_β values likely indicates a significant variation across the nebula, which could, for instance, be associated with mass loss variations or the dust ejected in the AGB phase (e.g. Walsh et al. 2016). Integral field spectroscopy should be very helpful to investigate the variation of c_β in both spatial directions of this nebula.

From the IC 4593's spectra it was possible to estimate the N_e and T_e using the diagnostic line ratios of sulphur, nitrogen and oxygen (see Table A1). Considering both slit positions, $T_e[O\ III]$ varies from (8100 ± 1800) K to (8800 ± 1100) K. Taking into account the uncertainties of T_e , our results are in agreement with the previously published values (for the literature references, see caption of Fig. 8). The only exception is the pair of LISs along 139° , which has higher values exceeding 11000 K. However, due to the large relative errors, we cannot argue for any variation in $T_e[O\ III]$ between the different components. In the case of $T_e[N\ II]$, the values computed in this work vary between 9510 K and 11400 K, again in agreement with the literature. Here as well, the LISs at $PA\ 139^\circ$ are characterized by higher values (~ 13000 K) and higher uncertainties. On the other hand, N_e is solely determined from the [S II] doublet lines and takes

¹ For further information about this tool and its error propagation, readers are directed to Wesson et al. (2012).

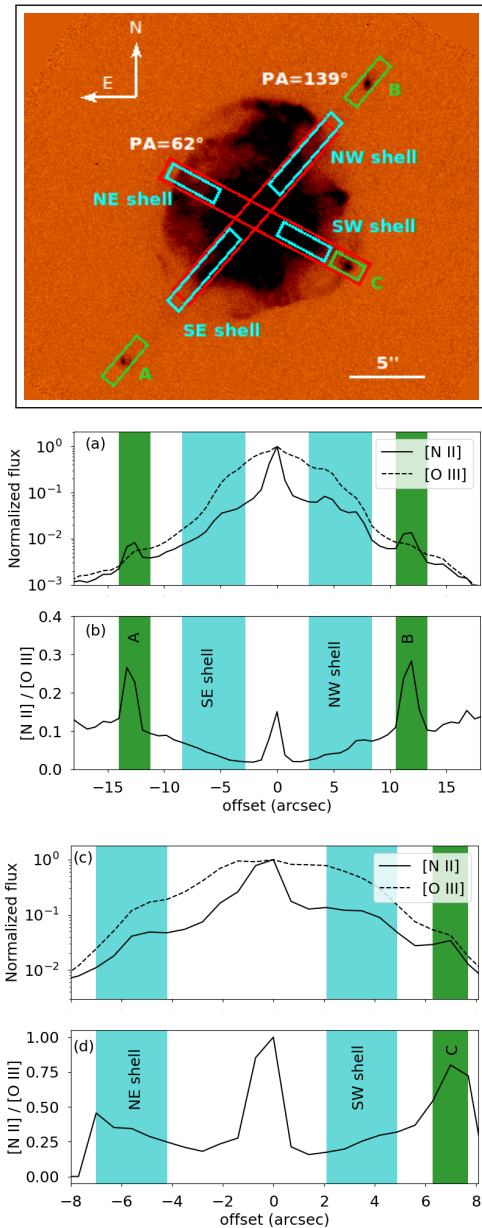


Figure 1. *Upper panel:* HST [N II] image of IC 4593. All regions and nebular components selected for the spectroscopic analysis, LISs, shells and Neb are highlighted with green, cyan and red coloured boxes, respectively. The extracted window of the LISs is 3.5 arcsec for the PA=139° slits (regions A and B) and 2.1 for the PA=62° slit (region C), for the shells is 3.5 arcsec for the slit at PA=62° and 6.3 arcsec for the slit at PA=139° and 15 arcsec for both Neb regions regardless the slit position. The size of the image is 30×25 arcsec². *Lower panels:* the flux distribution of the [N II] and [O III] emission lines, normalized to 1.0 – in logarithmic scale – and the [N II]/[O III] line ratio, along the slits at PA=139° (panels a and b) and PA=62° (panels c and d). The coloured regions correspond to the equivalent region/component in the upper panel.

values from $2100 \pm 1200 \text{ cm}^{-3}$ to $2800 \pm 600 \text{ cm}^{-3}$ that agrees with some published values, but is higher than others, as shown in Fig. 8. According to the analysis above, we can see that both T_e and N_e do not show any significant spatial variation among either the shells and LISs, or even from one to another PA (Neb).

The ionic and total abundances for IC 4593 are listed in Table A2.

No variation in He abundance between components is observed. The average value is 0.100 ± 0.004 , in good agreement with the majority of the literature (see Fig. 8), but lower than 0.11 reported by (Kwitter & Henry 1998) or 0.127 by Stanghellini et al. (2006). As for O/H, there is also no trend among nebular components, except for both LISs located along 139° that show lower values, variation related to the face values higher T_e [O III] of these LISs². Comparing with the published abundances, we note that our results of O/H are sometimes higher but, considering the errors, in agreement with Bohigas & Olgún (1996) and Stanghellini et al. (2006). For N/H our results are similar to those reported by Bohigas & Olgún (1996) and Kwitter & Henry (1998), and higher than those achieved in other works. Our results could indicate a possible variation in N/H abundances through the structures. However, Gruenwald & Viegas (1998) while analyzing the empirical abundances determinations, argued that abundances estimations through line intensities depend on the line of sight. Hence, the empirical abundances at different regions in a nebula may not be representative. In fact, we obtain a variation in the N/O abundance ratio, with the highest values found for the LISs along 139°. This result is, though, closely correlated with the problem of the much higher face values of the [O III] temperature, as discussed above. Ne/H abundances derived in this work are higher than in the literature. On the other hand, when performing the Ne/O ratio, the values fall close to those published by Barker (1978b); Bohigas & Olgún (1996); Stanghellini et al. (2006), within errors. Our Ar/H abundance is lower than the literature, while Cl/H abundance has not yet been reported. Following the criteria giving by Peimbert (1978) and Kingsburgh & Barlow (1994) to define Type I PNe – as $\text{He}/\text{H} \geq 0.125$ and $\text{N}/\text{O} \geq 0.5$ – this nebula is classified as non-Type I PN.

4.2 Hen 2-186

Hen 2-186 is a relatively small PN with an angular extension of $\sim 3.5''$. The $(\text{H}\alpha + [\text{N II}]) / [\text{O III}]$ ratio images from Corradi et al. (1996) have revealed a pair of LISs about $\sim 4.5''$ from the center, and oriented along 29° in position angle. The clump located near to the center of the nebula is actually a field star. Three components were selected for the analysis of this nebula: the pair of LISs and the inner nebula (Neb), all of them along the PA of 29° (see Fig. 2). This particular nebula belongs to a specific group of PNe, whose jets (LISs) have radial velocities greater than 100 km s^{-1} , with a value of 135 km s^{-1} (Corradi et al. 2000a; Guerrero et al. 2020b). Corradi et al. (2000a) suggested these LISs might be prominent point-symmetrical features within a more general structure containing faint bipolar lobes.

Table A3 shows the diagnostics derived for the different structures of the nebula. c_β of Hen 2-186 has an average value of 0.70 ± 0.04 , which agrees with the most recent estimation from Cavichia et al. (2010, $c_\beta = 0.75$), but is higher than that presented by Kaler (1970, $c_\beta = 0.4$) and lower than the value of 0.93 from Tylenda et al. (1992). The Neb component has a $T_e[\text{O III}]$ of $14600 \pm 330 \text{ K}$, slightly higher than $T_e[\text{N II}] = 11300 \pm 240 \text{ K}$. These figures coincide, within the uncertainties, with those presented so far in the literature (see Fig. 8). We were also able to derive $T_e[\text{O I}]$, though with larger uncertainty, as being $12700 \pm 3200 \text{ K}$. As for the N_e , we estimated

² We note that, at variance with T_e and N_e uncertainties, obtained directly from the propagation of the emission-line ones, the ionic and total abundance uncertainties were estimated via Monte Carlo approach, within NEAT. This is why X/H uncertainties seems to be small, even when the T_e uncertainties are severe.

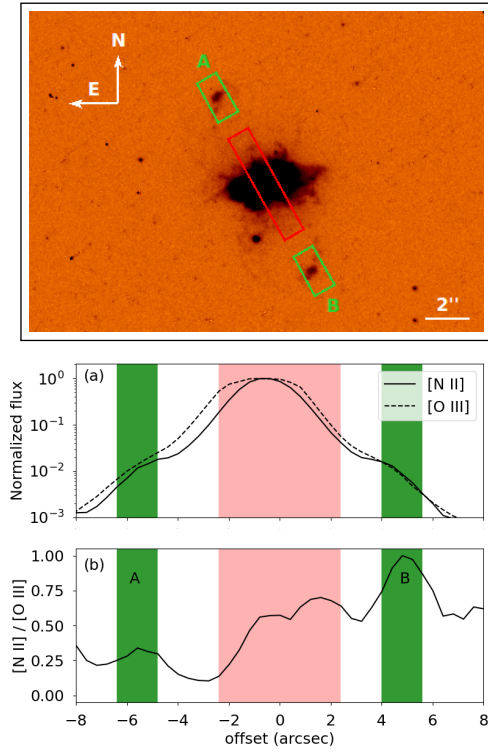


Figure 2. *Upper panel:* HST [N II] image of Hen 2-186. The size of the field is 20×14 arcsec². The nebular components under analysis are indicated by the boxes: the nebular region (Neb, 5.2 arcsec, in red) and the LISs (A and B, 2 arcsec, in green). *Lower panels:* Same as Fig 1.

$N_e[\text{Cl III}]$ of 8100 ± 1600 cm⁻³, $N_e[\text{Ar IV}]$ of 5420 ± 210 cm⁻³ and $N_e[\text{S II}]$ of 3990 ± 130 cm⁻³, for Neb. The latter is in good agreement with that reported by Cavichia et al. (2010). Taking into account the LISs and Neb T_e , we argue that Hen 2-186 does not reveal any important temperature spatial variation. With regard to the N_e , LISs are found to be less dense than Neb, by a factor between ~ 2.3 and ~ 3.7 . The higher densities found using the argon and chlorine line ratios may imply a density stratification in the inner nebula. Further spatially-resolved analysis is needed to confirm this trend.

Hen 2-186's ionic and total abundances are presented on Table A4. He abundances are found unchanged among the nebular components, with an average of 0.133 ± 0.009 , in good agreement with the literature (see Fig. 8). For the N abundance no variation is detected through the components, and the Neb result coincides with that published by Cavichia et al. (2010), but is lower than that reported by Ventura et al. (2017). Nonetheless, for O/H we can see that the LISs exhibit higher values than the nebula by a factor between ~ 2.1 and ~ 2.5 ³, and if errors are taken into account Neb value matches the published ones (see the caption of Fig. 8). A similar behavior is observed for Ne/H, for which LISs show higher abundances by a factor between ~ 1.9 and ~ 2.3 . With regard to Ar/H, it can be seen that it does not vary significantly among regions, and our estimations are lower than those reported in literature. On the other hand, the average of S/H abundance is similar to previous works. According to its chemical abundances, Hen 2-186 can be classified as non-type I PNe.

³ An over- or under-abundance of around two is not high enough to allow a firm conclusion of abundance variation across the nebula, due to the cavities of the ICF scheme (Kingsburgh & Barlow 1994; Delgado-Inglada et al. 2014).

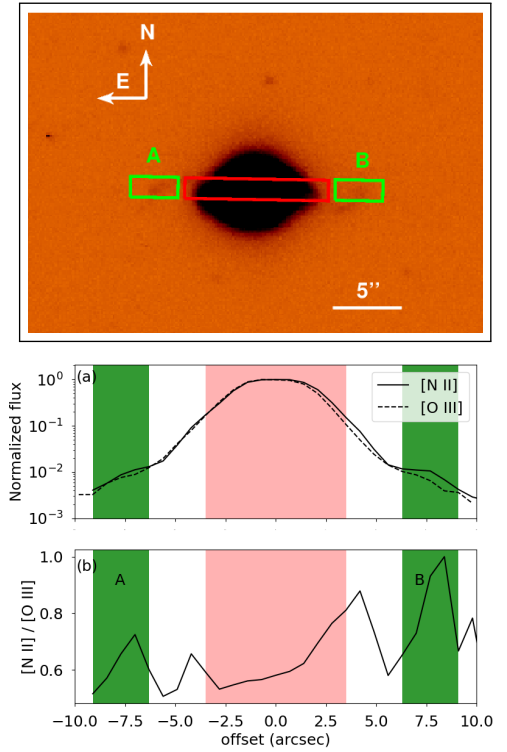


Figure 3. *Upper panel:* [N II] image of Hen 2-429 from Machado et al. (1996). The size of the field is 33×23 arcsec². The nebular components under analysis are indicated by the boxes: the nebular region (Neb, 10.5 arcsec, in red) and the LISs (A and B, 3.5 arcsec, in green). *Lower panels:* Same as previous Figures. Note: the bottom panel, which shows the line ratio, shows peaks that are not related to the features of the nebula, but to the displacement between spatial distribution of the emission lines. The [N II] and [O III] spectra are misaligned for a fraction of pixel, which generates the false peaks near the continuum, within the Neb region.

4.3 Hen 2-429

The PN Hen 2-429 possesses a point-symmetric morphology with an elliptical shell and a pair of faint jet-like features, the latter only prominent in low-ionization emission (Guerrero et al. 1999). These LISs are located at $\sim 6.5''$ from the center, oriented along the PA of 89° , and have systemic radial velocities of 5 km s⁻¹, according to Guerrero et al. (2020b). Our study of this nebula selects three components: the pair of LISs and the main body of the nebula (Neb), all of them along the position angle of 89° , as it can be seen in Fig. 3.

Our results in terms of the spectroscopic characterization (line intensities, $H\beta$ flux, c_β , N_e and T_e) of Hen 2-429's components are given in Table A5. As the table shows, its extinction coefficient is the highest in our sample, with an average value of 2.08 ± 0.09 , which agrees with (or is close enough to) the values reported in Giammanco et al. (2011, 2.12), Tylenda et al. (1992, 2.3) and Girard et al. (2007, 2.21). The electron temperatures of Hen 2-429 are provided only for Neb, $T_e[\text{O III}]$ of 9800 ± 2400 K and $T_e[\text{N II}]$ of 9400 ± 700 K, as neither the [N II] $\lambda 5755$ nor the [O III] $\lambda 4363$ auroral lines were detected in the LISs. Our estimations are consistent, within the errors, with the previous ones reported in the literature (see Fig. 8). As for N_e , we derived $N_e[\text{S II}]$ of 5710 ± 270 cm⁻³ and $N_e[\text{Cl III}]$ of 5200 ± 2400 cm⁻³ for the Neb component, values that are slightly smaller than previously reported. Compared to Neb, the N_e of the LISs are lower by a factor of ~ 1.8 and ~ 1.3 for A and B, respectively.

Ionic and total abundances are shown in Table A6. Taking into

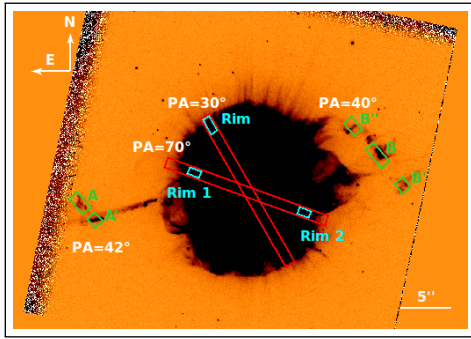


Figure 4. HST [N II] image of NGC 3918. The size of the field is 44×31 arcsec². The nebular components under analysis are indicated by the boxes: the nebular regions (Neb, same extension in all directions: 16.8 arcsec, in red); the rims (in cyan; for PA=30° 1.6 arcsec and for PA=70° 1.2 arcsec); the LISs (in green; for A 2 arcsec, for A' 1.2 arcsec, for B 2.4 arcsec, for B' 1.2 arcsec and for B'' 1.6 arcsec).

account the errors, Neb abundances are in good agreement with [Girard et al. \(2007\)](#), with the exception of He/H for which our value (0.151 ± 0.019) is higher than the published one (see Fig. 8). As it can be seen in Table A5, no electron temperature was computed for the LISs. However, the abundances of LISs were estimated adopting the mean- and low-ionization temperatures of the Neb. Within the uncertainties, we find no significant variation of abundances between LISs and Neb. Values on Table A6 allow us to classify Hen 2-429 as non-type I PN.

4.4 NGC 3918

NGC 3918 is a widely studied planetary nebula and characterized by a complex morphology – various models have been used to reproduce its morphological properties. [Clegg et al. \(1987\)](#) proposed a biconical geometry, whereas [Ercolano et al. \(2003\)](#) adopted, besides the biconical one, two spindle-like models. Both representations have integrated emission-line spectra which are in agreement with the observations. [Peña et al. \(2017\)](#) came to the conclusion that NGC 3918 has a complex point-symmetric morphology. Aside from the large-scale structures, it has LISs located outside the main PN body and oriented approximately along the major axis. ($H\alpha + [N II]$)/[O III] ratio images from [Corradi et al. \(1996\)](#) initially revealed the presence of one jet and one knot on radially opposite sides. In this work, we present the spectroscopic analysis of several NGC 3918's structures, by adopting the nomenclature defined by [Corradi et al. \(1999\)](#), including also two other micro-structures named B' and B''. All nebular components under our analysis are shown in the HST [N II] image of the nebula in Fig. 4.

The properties that the present data allow us to derive, for the different nebular components, are shown in Table A7. Note that the recombination lines of C II at $\lambda 4267 \text{ \AA}$, C III at $\lambda 4647 \text{ \AA}$ and C IV at $\lambda 5801/12 \text{ \AA}$ are detected in our spectra and also reported by [Clegg et al. \(1987\)](#) and [Górný \(2014\)](#). In the latter, these recombination lines were considered as *mimics of emission-line stars*. As [Górný \(2014\)](#), we also suggest that the origin of these lines is not stellar, and base our argument on their spatial distribution in the 2D spectra (see Fig. 5).

The interstellar extinction of NGC 3918 has an average value of 0.28 ± 0.01 , without a significant variation among the different structures. Our value is lower than those obtained by [Pena & Torres-Peimbert \(1985\)](#), [Tsamis et al. \(2003\)](#), and [Robertson-Tessi & Garnett \(2005\)](#), which amount to 0.40, 0.44 and 0.40, respectively. Neverthe-

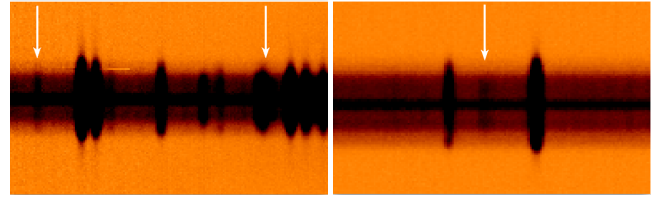


Figure 5. Two different regions of the 2D spectra of NGC 3918 to highlight the mimics of emission-line stars. *Left panel:* the arrows correspond to the lines of C II at $\lambda 4267 \text{ \AA}$ (left) and C III at $\lambda 4647 \text{ \AA}$ (right). *Right panel:* the arrow indicates the position of the C IV at $\lambda 5801/12 \text{ \AA}$ line.

less, our result is consistent, within the uncertainties, with the values found in [Clegg et al. \(1987\), \$0.33 \pm 0.14\$ \(using the Balmer decrement\), \[Kwitter et al. \\(2003\\), 0.27\\) and \\[García-Rojas et al. \\\(2015\\\), \\\$0.26 \pm 0.06\\\$. \\\$N_e\\\$ and \\\$T_e\\\$ were estimated using the diagnostic line ratios of sulphur, chlorine, argon, nitrogen and oxygen. No significant variation is found for \\\$T_e\\\$ \\\[N II\\\] among the different structures. For Neb we obtained \\\$T_e\\\$ \\\[N II\\\] of \\\$11100 \pm 500\\\$ K, along 30°, and \\\$11200 \pm 800\\\$ K for the PA of 70°, both agree well with the literature. The average value of \\\$T_e\\\$ \\\[O III\\\] for Neb is \\\$12700 \pm 140\\\$ K, which is also in good agreement with the published values. This latter temperature also has no significant variation across the nebular components, though LIS B'', along the PA of 40°, has higher \\\$T_e\\\$ \\\[O III\\\] face values, with far higher errors than the other structures. As for the \\\$N_e\\\$, we computed \\\$5230 \pm 190 \text{ cm}^{-3}\\\$, \\\$5700 \pm 800 \text{ cm}^{-3}\\\$ and \\\$4220 \pm 80 \text{ cm}^{-3}\\\$ as the average values for Neb, from the \\\[S II\\\], \\\[Cl III\\\] and \\\[Ar IV\\\] diagnostic lines, respectively. \\\$N_e\\\$ \\\[S II\\\] is consistent with the literature, but lower than the value determined by \\\[Richer et al. \\\\(1991\\\\), \\\\$5700 \text{ cm}^{-3}\\\\$ and higher than that of \\\\[Kwitter et al. \\\\\(2003\\\\\), \\\\\$3800 \pm 380 \text{ cm}^{-3}\\\\\$. The mean value of \\\\\$N_e\\\\\$ \\\\\[Cl III\\\\\] is also in good agreement with the literature, whereas for the case of \\\\\$N_e\\\\\$ \\\\\[Ar IV\\\\\] our value is lower than those published by \\\\\[Stanghellini & Kaler \\\\\\(1989\\\\\\)\\\\\]\\\\\(#\\\\\) and \\\\\[García-Rojas et al. \\\\\\(2015\\\\\\)\\\\\]\\\\\(#\\\\\), of \\\\\$6166 \text{ cm}^{-3}\\\\\$ and \\\\\$6500^{+1300}_{-1200} \text{ cm}^{-3}\\\\\$, respectively. Regarding the variation among different nebular components, it should be noted that for the case of LISs, the \\\\\$N_e\\\\\$ could only be calculated using the sulfur diagnostic lines that, in comparison with Neb, is lower by a factor that varies from \\\\\$\sim 2.6\\\\\$ to \\\\\$\sim 3.9\\\\\$.\\\\]\\\\(#\\\\)\\\]\\\(#\\\)\\]\\(#\\)\]\(#\)](#)

Ionic and total abundances are listed in Table A8, from which no variation in He abundances is observed. The average He/H is 0.104 ± 0.003 , in good agreement with the literature (see Fig. 9). For O/H there is no much contrast among nebular components, except for the LIS B'', along 40°, for which we find a value of approximately half that of the other structures. Similarly to the case of IC 4593, this under-abundance of B'' is related with the much higher, and much uncertain, T_e [O III]. Excluding this LIS, the average O/H is $(4.0 \pm 0.1) \times 10^{-4}$, which is lower than those obtained previously by some authors, but considering the errors agrees with [Henry et al. \(2018\)](#). The N/O abundance ratio also agrees with the published values in the literature. Considering the quantities in Table A8, we conclude that this nebula classifies as non-type I. The neon abundance behaves as O/H, without any variation among nebular components (with the exception of B'', whose value is lower than the average of the other structures, by a factor ~ 5.7). Given that B'' is the faintest nebular component of NGC 3918, and also the fact the its behaviour differs significantly from that of the other LISs of the nebula, we do not argue that the variation in either T_e or X/H is real. At variance with Ar abundance, the average Cl/H and S/H are consistent with those published by [Kwitter et al. \(2003\)](#).

4.5 NGC 6543

NGC 6543 is among the most widely studied PNe and several works have focused on understanding its complex morphology (e.g. Balick et al. 1987; Miranda & Solf 1992; Balick et al. 1994; Reed et al. 1999; Ramos-Larios et al. 2016; Guerrero et al. 2020a) concluding that it is formed by a geometrically thick expanding ellipsoid with two bright shells. NGC 6543 also possesses a pair of LISs with radial velocities of 39 km s^{-1} (Miranda & Solf 1992; Reed et al. 1999; Guerrero et al. 2020b). Moreover, recent near-IR narrow-band imagery of the nebula has revealed the presence of H_2 emission in the $[\text{N II}]$ emission between the rims/shells and LISs (Akras et al. 2020b).

The analysis we present here follows the same nomenclature proposed by Miranda & Solf (1992). Our study is based on two slit positions (5° and 163°), and the nebular components under analysis are denoted as A, D and J (in the northern half), with their counterparts A', D', J', and Neb. The J and J' LISs are covered by the slit at PA of 5° (see Fig. 6).

Table A9 shows the line intensities, observed $\text{H}\beta$ flux, c_β , N_e and T_e derived for the above structures, along both slits. From Table A9 it is straightforward noticing that c_β varies among the components, from ~ 0.02 up to 0.26. The average extinction coefficient is 0.11 ± 0.02 , which is in good agreement with Perinotto et al. (1999, 0.12) and Williams et al. (2008, 0.14). Interestingly, c_β values in the range from 0.08 up to 0.3 have also been reported by other authors as Robertson-Tessi & Garnett (2005, 0.08), Wesson & Liu (2004, 0.1), Kaler (1970, 0.22) and Hyung et al. (2000, 0.3). As in the case of IC 4593, this non-negligible variation in c_β points to spatial variations within the nebula. Such a spatial variation is also obtained, for instance, from the 2D c_β map of NGC 7009 computed for MUSE IFU data (Walsh et al. 2018).

For the estimation of electron temperature and density, the diagnostic line ratios of sulphur, chlorine, argon, nitrogen and oxygen were used. Considering all nebular components, except the LISs, along both slit positions, the computed average value of $T_e[\text{O III}]$ is $8150 \pm 210 \text{ K}$ in very good agreement with the literature (see Fig. 9). As for the J and J' (LISs), $T_e[\text{O III}]$ is $12100 \pm 7500 \text{ K}$ and $10000 \pm 7000 \text{ K}$, respectively. These results may be indicative of extra heating mechanisms, such as shocks. However, the much higher uncertainties obtained for the LISs' do not allow firm conclusions about the possibility of real variations of $T_e[\text{O III}]$ among the nebular components. Regarding the $T_e[\text{N II}]$ of components A, A', D and D', we obtain an average value of $10000 \pm 500 \text{ K}$, in good agreement with previous estimations. As for the J and J' contrast with the other components, the errors again prevent robust conclusions. Balick et al. (1994) also studied three different regions of this nebula, named rim, cap and ansae (the latter are equivalent to our LISs), with a long-slit along the position angle of 14° . Balick et al. (1994) electron temperatures for the three structures are $T_e[\text{O III}]$ ($T_e[\text{N II}]$) of 8000 K (9300 K), 7900 K (9000 K) and 8200 K (7400 K), respectively. Therefore, for the rim and cap components their values are coincident with ours, while for the ansae our results are higher, with higher uncertainties, though strictly speaking, ours and Balick et al. (1994) derived quantities are in good agreement.

Sulfur, chlorine and argon lines allowed the derivation of the electron densities. A subtle variation is found among the nebular components, but J/J', the LISs, are showing much lower electron densities. In particular, the average value for $N_e[\text{S II}]$ is $5060 \pm 100 \text{ cm}^{-3}$ for the slit at along 5° and $5220 \pm 130 \text{ cm}^{-3}$ for the 163° one. As for the J and J' LISs, we determined $N_e[\text{S II}]$ of $950 \pm 240 \text{ cm}^{-3}$ and $930 \pm 210 \text{ cm}^{-3}$, respectively. These values are lower when compared to the other components, by factors of ~ 5.3 for J and ~ 5.5 for J'. The

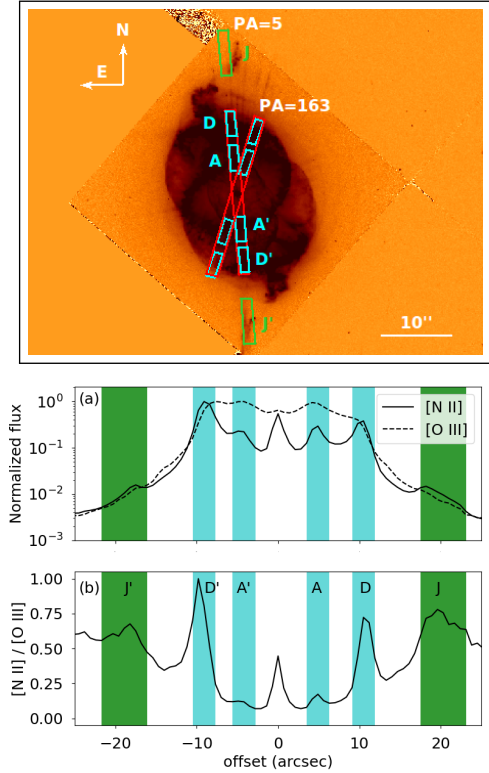


Figure 6. Upper panel: HST $[\text{N II}]$ image of NGC 6543. The size of the field is $63 \times 48 \text{ arcsec}^2$. The nebular components under analysis are indicated by the boxes: the nebular regions (Neb, same extension in both directions: 23.1 arcsec, in red); the shells (A, A', D, D', 3.5 arcsec in cyan); the LISs (J and J', 6.3 arcsec, in green). Lower panels: Same as previous Figures, along the slit which contains the LISs, PA= 5° .

comparison with the literature shows that our densities are close to the previous calculations (see Fig. 9). Moreover, Balick et al. (1994) computed the electron density for the rim, cap and ansae obtaining 4600 cm^{-3} , 5000 cm^{-3} and 2200 cm^{-3} , respectively. $N_e[\text{Cl III}]$ and $N_e[\text{Ar IV}]$ were also computed for the main nebular structures (Neb) and their average are $4630 \pm 310 \text{ cm}^{-3}$ and $6800 \pm 900 \text{ cm}^{-3}$, respectively. The resultant values again are in agreement with the previous estimations of $N_e[\text{Cl III}]$ of Wesson & Liu (2004, 4660 cm^{-3}) and Williams et al. (2008, $5000^{+2100}_{-1400} \text{ cm}^{-3}$), but slightly larger than $N_e[\text{Ar IV}]$ of Robertson-Tessi & Garnett (2005, $5020 \pm 800 \text{ cm}^{-3}$) and Williams et al. (2008, $4500^{+1100}_{-900} \text{ cm}^{-3}$).

Table A10 shows the derived values of the ionic and total abundances. He abundances are spread within the range from 0.098 ± 0.002 to 0.124 ± 0.024 for the different nebular components. Hyung et al. (2000) studied two regions of this nebula (named *east* and *north*) and they found a similar helium abundance behaviour of 0.1 and 0.13, respectively, for these two regions. Though no errors are quoted for the latter results, authors argue that this dissimilitude gives room for a possible spatial variation in the nebula. For the O abundance, there is no trend among nebular components, and our results are in agreement with published values (see Fig. 9), except for both LISs located along the position angle of 5° . The latter have slightly lower oxygen abundances, which are actually on the limit to, within the errors, agree with that of the other components. As far as N/H is concerned, there could be a very small variation across the nebula, with the highest values found in the A and D rims, together with the J' LISs (all along the same PA, 5°), possible variation that was also reported

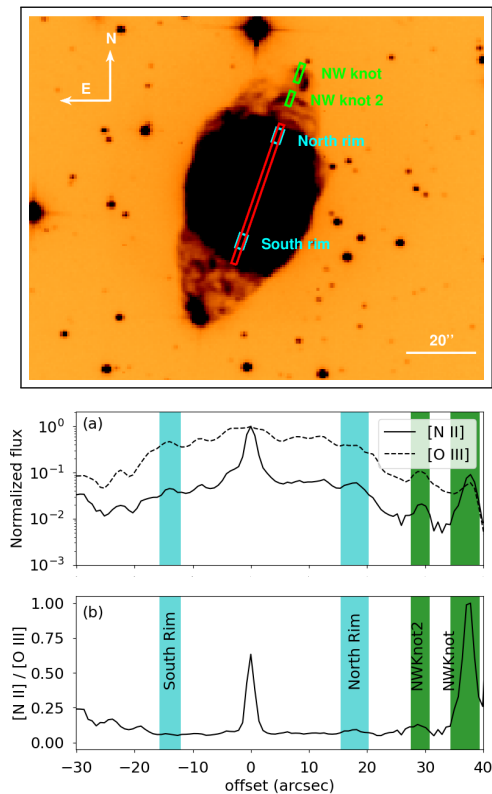


Figure 7. Upper panel: $H\alpha + [N \text{ II}]$ image of NGC 6905 from Corradi et al. (2003). The size of the field is $130 \times 104 \text{ arcsec}^2$. The nebular components under analysis are indicated by the boxes: the nebular region (Neb, 42 arcsec, in red); the rims (4.2 arcsec for south and 5.6 arcsec for north one, in cyan); the LISs (5.6 arcsec for NW knot and 4.2 arcsec for NW knot2, in green). Lower panels: Same as previous Figures.

by Balick et al. (1994). The Ne abundance also follows the possible small variation through the components (peaking at the position of the rims AA' and DD') and in average it is in good agreement with the literature. Considering the average of N/O and He/H, we conclude that this nebula is of non-Type I class. The total Ar abundances present some subtle variations, being the lowest in the DD' (rim) and invaluable for the LISs. For Neb, Ar/H is sub-estimated by one order of magnitude, when compared with some authors, but close to the values reported by Perinotto et al. (2004), as it can be seen in Fig. 9.

4.6 NGC 6905

This nebula has a bright, broadly spheroidal shell, with a roughly conical shape extending over $\sim 82 \text{ arcsec}$, with a pair of LISs located $\sim 35''$ from the central star. The $H\alpha + [N \text{ II}]$ images from Corradi et al. (2003) reveal this pair of LISs, and also another one near the NW LIS, which we refer to as NW knot 2. The opposite knot of the pair (SE knot) is close enough to a field star to be contaminated, so it was excluded from our spectroscopic analysis. The nebular components that we selected for analysis are shown in Fig. 7, while the results of their analysis appear in Table A11.

The interstellar extinction coefficient of NGC 6905 does not show significant variation from one to another nebular component, with an average of 0.05 ± 0.02 . Our c_B agrees with one of the previous works, 0.11 ± 0.18 (Cahn 1976). Other authors reported extinctions of 0.27 (Kingsburgh & Barlow 1994, for a PA of 90°) or 0.23, 0.22, 0.29 (Pena et al. 1998, three different slit positions), 0.55 (Kaler 1970) and

0.93 (Kaler 1986). In fact, recently Gómez-González et al. (2022) studied almost the same low- and high-ionization structures as in the present work (and named A1, A2 and A3 our NWknot, NWknot2 and north rim, as well as A6 for our south rim), by using longslit spectra with a PA of 155° . These authors also obtain a similar c_B variation, from 0.05 to 0.23.

We did not find significant difference in $T_e[\text{O III}]$ among the structures, being the mean $13960 \pm 1088 \text{ K}$. This temperature is higher than some previous measurements (see Fig. 9), but close to that of Kaler (1970, 14300 K). Gómez-González et al. (2022) obtained $T_e[\text{O III}]$ of $12840 \pm 1010 \text{ K}$ for A1, $12430 \pm 800 \text{ K}$ for A2, $12030 \pm 380 \text{ K}$ for A3 and $12930 \pm 440 \text{ K}$ for A6, all comparable with ours (nevertheless the central value we found for NWknot is a factor ~ 1.3 higher). Pena et al. (1998) also studied this nebula using three different positions angles: (i) 90° , passing through the central star; (ii) 0° , with $5''$ offset to the north of the central star; and (iii) 90° for the SE LIS. Their $T_e[\text{O III}]$ of $(12100 \pm 800) \text{ K}$, $(13100 \pm 800) \text{ K}$ and $(14000 \pm 3000) \text{ K}$ for each of these slits, respectively, are not in disagreement with our mean $T_e[\text{O III}]$. Notice that a spatial variation in $T_e[\text{O III}]$ may be indicated from the $T_e[\text{O III}]$ of Pena et al. (1998), but the uncertainties do not allow for a robust conclusion. An analysis of c_B and T_e with IFU will be useful to further investigate the possibility of their spatial variation in NGC 6905. As for the electron density, the Neb value we derived from the $[\text{S II}]$ doublet is $(740 \pm 150) \text{ cm}^{-3}$, whereas densities of the rims are much lower having values of 350 ± 80 and 280 ± 40 , and LISs are less dense by a factor of ~ 2.5 and ~ 3.4 . Yet, the Neb density agrees, within the errors, with Stanghellini & Kaler (1989, 850 cm^{-3}), but it is lower than that of Pena et al. (1998, 1500 cm^{-3}). Regarding the LIS, despite the fact that both sulfur diagnostic lines were detected, the line ratios lies outside the theoretical curve (e.g. Osterbrock & Ferland 2006; Stanghellini & Kaler 1989), indicating a very low electron density. Thus, we argue for $N_e[\text{S II}] < 220 \text{ cm}^{-3}$ for NW knot. Accounting for the errors, Gómez-González et al. (2022) LISs ($500 \pm 290 \text{ cm}^{-3}$) and north rim ($480 \pm 220 \text{ cm}^{-3}$) densities are also in agreement with our results.

NGC 6905 abundances are listed in Table A12. As expected, there is no variation in He abundance from one to another component, being $\text{He}/\text{H} = 0.118 \pm 0.038$, the average value, in agreement with previous literature reports (see Fig. 9). It should be noted that a strong variation in the $\text{He II } \lambda 4686/\text{H}\beta$ has been reported by Vorontsov-Vel'Yaminov (1961), with an intensity ratio varying from 0.5 to 1.3 over ~ 15 years (between 1945 and 1959). In our analysis we find, for Neb, a $\text{He II } \lambda 4686/\text{H}\beta$ ratio of ~ 1.05 . Gómez-González et al. (2022) succeed in separating the central star from the nebular emission. Ours and theirs $\text{He II } 4686 \text{ \AA}$ for both structures match well, apparently indicating both emissions are blended. With the exception of the NW knot, for which we find an under-abundance of a factor ~ 2.8 respect to the Neb, the O/H does not change among the components. Per structure, N/H are higher than those reported by Gómez-González et al. (2022), which may be due to need of applying the $T_e[\text{O III}]$ instead of $T_e[\text{N II}]$ to derive the nitrogen abundance. On one hand, N/O is similar throughout the nebular components, but, on the other hand, higher in the NW knot by a factor ~ 1.4 . Considering He/H and N/O in Table A12, we can conclude that NGC 6905 classifies as Type I. The total Ne/H abundances are also similar among the nebular components and in agreement with the values reported in literature. On the other hand, Ar/H presents a variation with the higher value found for one of the rims (also higher than in the literature, as in Fig. 9) but not measurable for NW knot. S/H is found to be nearly constant among the nebular components except the NW LIS, for which it is lower by a factor of ~ 3.2 respect to the Neb, difference

that was also reported by Gómez-González et al. (2022). As in the case of a couple of LISs previously mentioned, some X/H are lower in the LIS than in the rest of the components, as a consequence of the $T_e[\text{O III}]$ that is also much higher (and highly uncertain).

5 DISCUSSION

In the following we discuss different aspects of the physical, chemical and excitation properties of the six PNe whose results were given above, focusing on their variation across slits and/or components, and also allowing for the comparison with the literature.

5.1 Extinction variation

For two of the PNe in the sample we found variations in the extinction coefficient. The first case is IC 4593, for which this coefficient is ranging from 0.02 ± 0.02 to 0.22 ± 0.01 . We also want to note that the intensities of H γ and H δ lines display a small variation from one another structure, suggesting a real internal spatial variation in this coefficient. The second case is NGC 6543, which has a c_β that takes values from 0.02 ± 0.02 to 0.26 ± 0.01 . For this nebula, there is a PA in which the H α line was saturated, therefore c_β was estimated using only H γ and H δ . Even so, the other PA studied, whose c_β were calculated also using H α , presents as well extinction coefficient variations. As with the previous nebula, we note that the intensity of H γ and H δ lines show small variation. In addition, in recent works of Akras et al. (2020a) and Akras et al. (2022), in which longslit were simulated on IFU data, the authors verify that variations in the extinction coefficient are present even as a result of only changing the PA. Therefore, these spatial variations in the extinction coefficient, in both nebulae, are likely real, and they can only be much better studied through IFU data.

5.2 Densities and temperatures

Figure 10 displays $N_e[\text{S II}]$ as a function of T_e from the [N II] (upper panel) and the [O III] (lower panel) lines. The main conclusions drawn from these plots are: (i) $T_e[\text{N II}]$ is almost invariant through the components considering their uncertainties, whereas LISs' $T_e[\text{O III}]$ is higher compared to the rims/shells, although the large uncertainties do not allow for a robust conclusion; and (ii) $N_e[\text{S II}]$ is generally lower for LISs relative to the rest of the components.

The comparison between the two T_e indicators – from [N II] and [O III] lines – is presented in Fig. 11. In particular, we find that the mean value for $T_e[\text{N II}]$ is 11000 ± 1600 and $T_e[\text{O III}]$ is 12600 ± 1200 K for the group of LISs, whereas for the group of rims/shells these values are 10200 ± 800 and 9510 ± 220 K, respectively. This difference in T_e between the two indicators is also present for the sample of PNe discussed by Osterbrock & Ferland (2006) (see their Fig.5.3) and attributed to excitation differences among the nebulae.

5.3 Abundance trends

Fig. 12 shows that the range of $\log(\text{N}/\text{H})$ and $\log(\text{O}/\text{H})$ we derived are -4.4 to -3.0 and -4.2 to -3.0 , respectively. A negligible variation in $\log(\text{N}/\text{H})$, for $T_e[\text{N II}]$, was observed, regardless the nebular components. On the contrary, the derived O abundances show a non-negligible variation with $T_e[\text{O III}]$. In particular, most of $\log(\text{O}/\text{H})$ lie within the range of -3.6 to -3.1 , regardless of $T_e[\text{O III}]$. But there are four cases with $\log(\text{O}/\text{H}) < -3.7$: two LISs in IC 4593, one

Table 2. General characteristics of central star planetary nebulae (CSPNe) from Weidmann et al. (2020).

	Type	T_{eff} [K]	L [L_\odot]	$\log(g)$
IC 4593	O(H)5f	~ 48000	~ 5500	3.70
Hen 2-186	Cont. [†]	~ 107500	~ 7900	5.40
Hen 2-429	[WC 4] ⁽¹⁾	~ 23000 ^{††}	~ 5900	-
NGC 3918	O(H)	~ 150000	~ 5000	5.56
NGC 6543	Of-WR(H) ⁽²⁾	~ 60400	~ 3800	4.70
NGC 6905	[WO 2] ⁽³⁾	~ 130900	~ 10200	4.70

Notes: [†] Type *cont.* means that its spectrum has a high S/N ratio with no stellar features. ^{††} Such a low temperature contradicts our spectroscopic data in which we detect the He II $\lambda 4686$ line.

⁽¹⁾ We detected emission lines from this type of CSPN (see Table A5) having FWHM in good agreement with the literature De Araujo et al. (2002, 37 \pm 1).

⁽²⁾ We identify emission lines with a stellar origin (see Table A9).

⁽³⁾ According to Aller (1968) and Cuesta et al. (1993), this nebula owns one of the most broadened O VI emission lines observed among PNe, which are also detected in our spectra (see Table A11) and reported by Gómez-González et al. (2022)

LIS in NGC 3918 and one in NGC 6905. The latter cases are also characterized by $T_e[\text{O III}] > 15000$ K, which is thus responsible for the resulting lower O abundances relative to the rest of the components in these PNe. Notice that all these cases are also described by very large uncertainties in $T_e[\text{O III}]$ due to the detection of weak [O III] 4363Å emission line.

Figure 13 presents the correlation among various abundance ratios. The dashed lines in the He/H versus $\log(\text{N}/\text{O})$ plot, define the limits of Type I PNe ($\text{He}/\text{H} \geq 0.125$ and $\log(\text{N}/\text{O}) \geq -0.3$, Peimbert 1978). All but one PNe (NGC 6905) are classified as non-Type I. The $\log(\text{N}/\text{H})+12$ versus $\log(\text{N}/\text{O})$ plot gives the best linear relation as $\log(\text{N}/\text{O}) = 0.85(\log(\text{N}/\text{H}) + 12) - 7.37$, with a goodness-of-fit (R^2) equal to 0.83, if eliminating the LISs marked with arrows (the same highlighted in Fig. 12). Our analysis returns a slightly different slope and intercept when compared to a sample of PNe with [WR]-type central stars (0.73 and -6.50 , García-Rojas et al. 2013) or a sample of PNe with LISs (0.74 and -6.50 , Paper I).

The correlations between $\log(\text{X}/\text{H})+12$ and $\log(\text{X}/\text{O})$ for X = Ar, Ne, S and Cl are also presented in Fig. 13. No significant contrast between LISs and the rims/shells are found for these chemical abundances, in agreement with the conclusions from Paper I, and other previously published analyses.

5.4 Central star properties

Concerning the central stars of the PNe studied here (Table 2), we find that these PNe containing LISs have either [WR]- or O(H)-type (see also, Miszalski et al. 2009) covering a large range of T_{eff} , ~ 45000 K to ~ 150000 K, L ranging from $\sim 3800 L_\odot$ up to $\sim 10000 L_\odot$, and $\log(g)$ taking values from 3.7 to 5.5.

5.5 Photo- versus shock-excitation of LISs

The long-standing problem of the excitation mechanism of LISs can also be addressed for our sample of PNe. In Paper I, the $f_{\text{shocks}}/f_{\text{star}}$ ratio was defined to explore the contribution of shocks on LISs and their host PNe. This ratio describes the ionizing photon flux emitted from the central star (f_{star}) and the ionizing photon flux produced by a potential shock interaction (f_{shocks}). Paper I authors

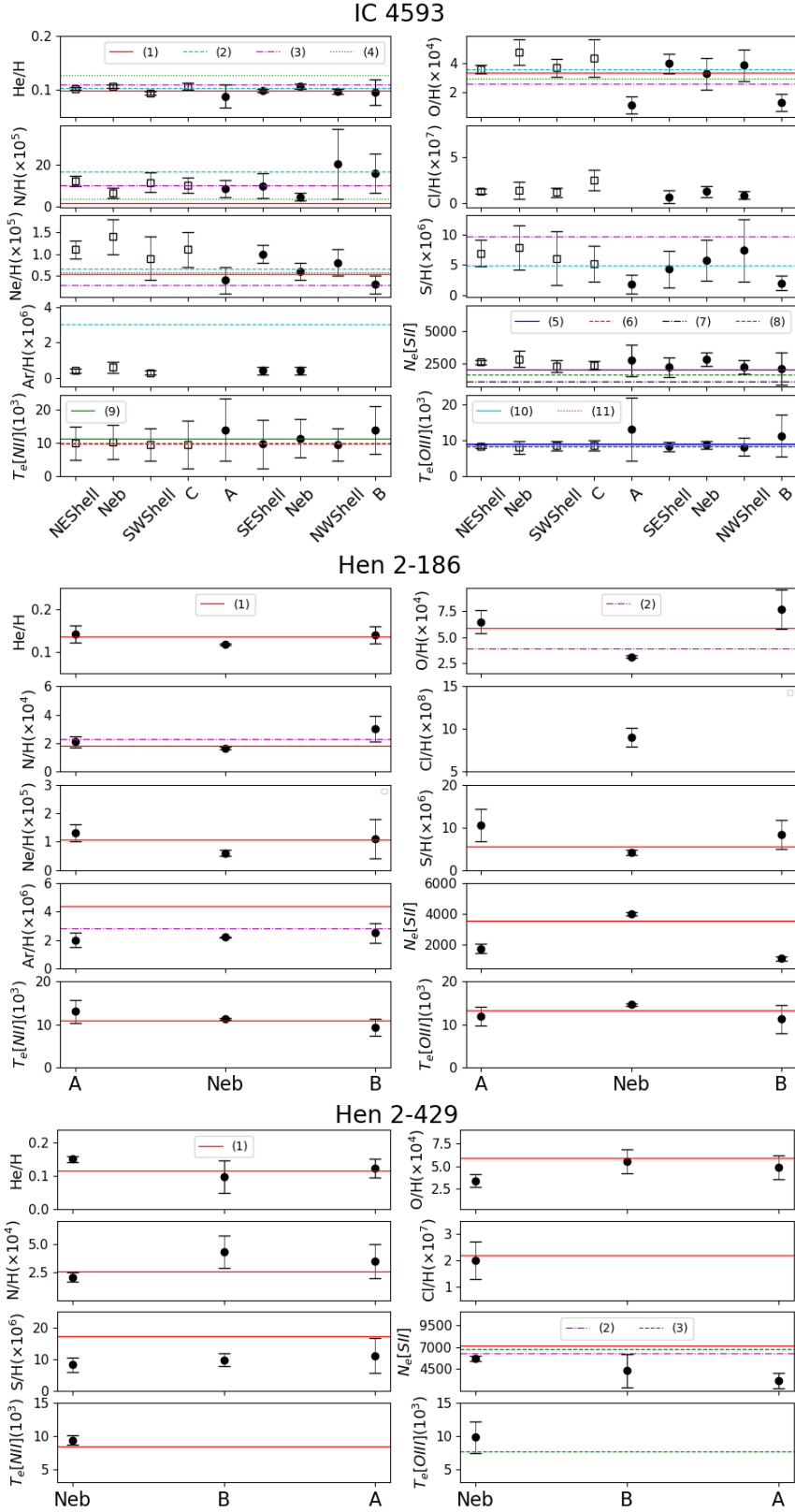


Figure 8. Variation of total abundances, electronic density and temperature across nebular components for IC 4593, Hen 2-186 and Hen 2-429. The horizontal lines represent values published in the literature, only for comparison with our results. When a studied nebula has more than one PA, different symbols represent different PAs. References for IC 4593: (1) Perinotto (1991), (2) Bohigas & Olguín (1996), (3) Kwitter & Henry (1998), (4) Stanghellini et al. (2006), (5) Barker (1978a), (6) Delgado Inglada et al. (2009), (7) Stanghellini & Kaler (1989), (8) Phillips (1998), (9) Kaler (1978), (10) Kaler (1978), (11) Robertson-Tessi & Garnett (2005). References for Hen 2-186: (1) Cavichia et al. (2010), (2) Ventura et al. (2017). References for Hen 2-429: (1) Girard et al. (2007), (2) Górný & Tylenda (2000), (3) Medina et al. (2006).

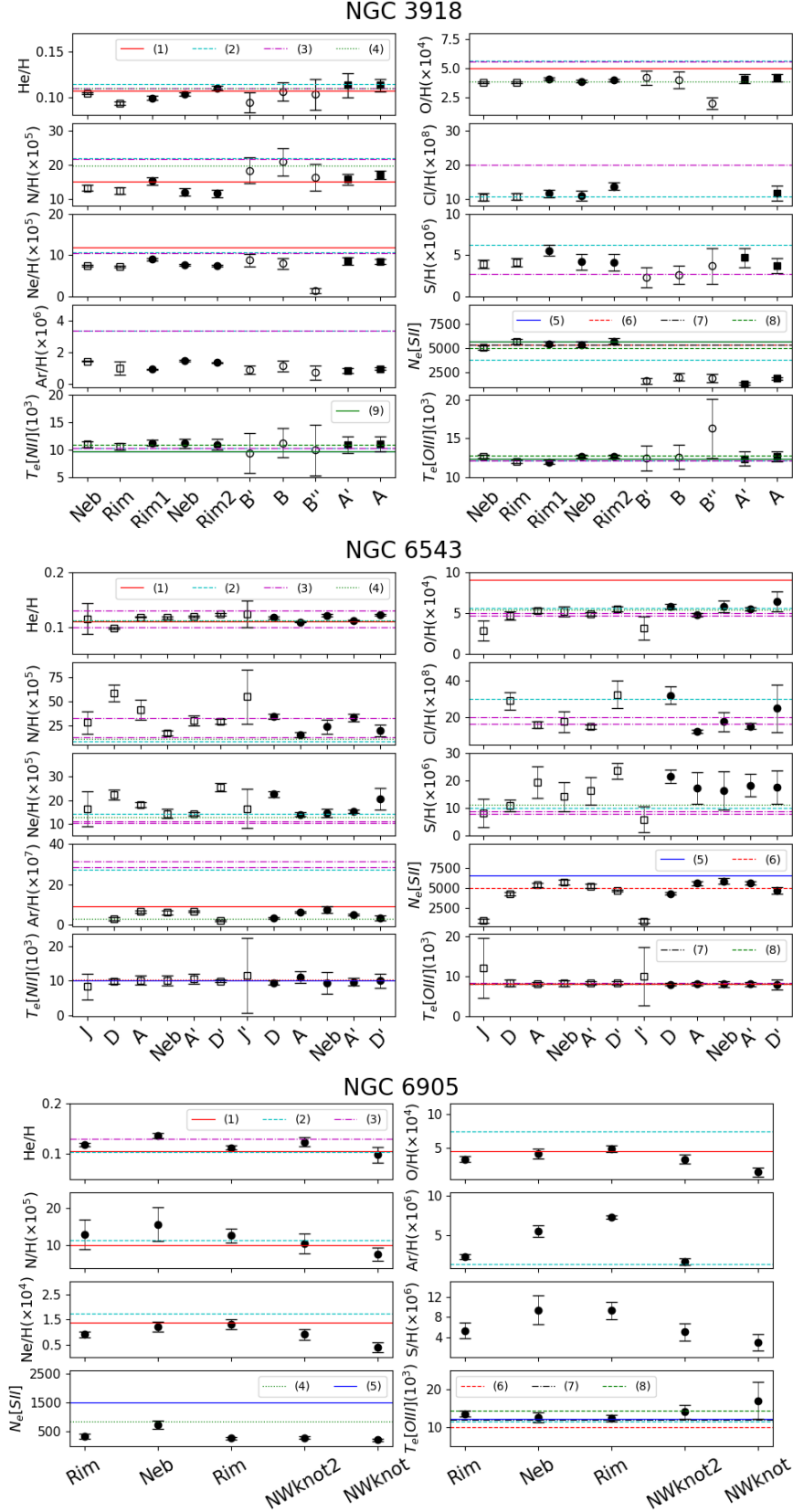


Figure 9. Same as Fig. 8 for NGC 3918, NGC 6543 and NGC 6905. References for NGC 3918: (1) Perinotto (1991), (2) Kwitter et al. (2003), (3) Henry et al. (2004), (4) Henry et al. (2018), (5) Clegg et al. (1987), (6) Stanghellini & Kaler (1989), (7) Phillips (1998), (8) García-Rojas et al. (2015), (9) Richer et al. (1991). References for NGC 6543: (1) Kaler (1970), (2) Perinotto et al. (1999), (3) Hyung et al. (2000), (4) Perinotto et al. (2004), (5) Wesson & Liu (2004), (6) Williams et al. (2008), (7) Phillips (1998), (8) Robertson-Tessi & Garnett (2005). References for NGC 6905: (1) Perinotto (1991), (2) Kingsburgh & Barlow (1994), (3) Stanghellini et al. (1995), (4) Stanghellini & Kaler (1989), (5) Pena et al. (1998), (6) Cahn (1976), (7) Kaler (1986), (8) Kaler (1970).

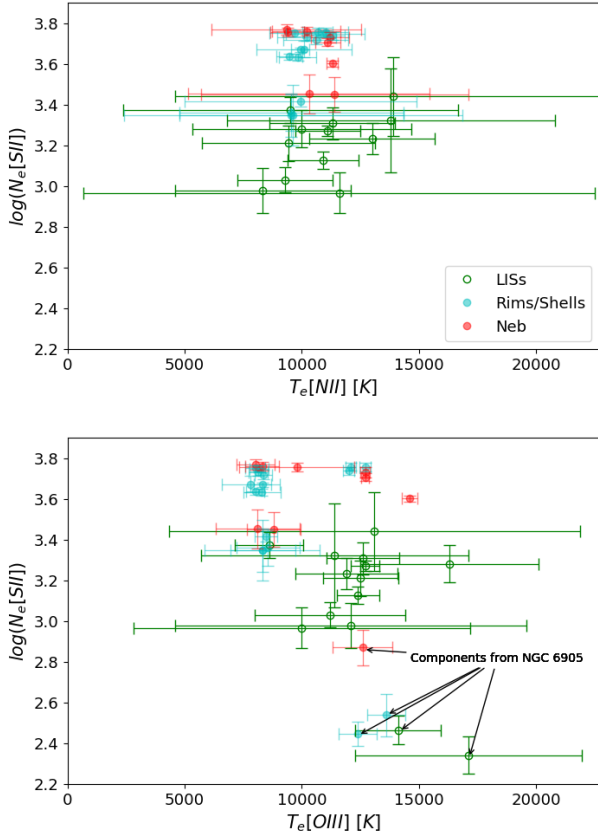


Figure 10. T_e versus N_e for all the components in our PNE’s sample. *Upper panel:* T_e using [N II] diagnostic lines versus $\log(N_e[\text{S II}])$. *Lower panel:* T_e using [O III] diagnostic lines versus $\log(N_e[\text{S II}])$. Arrows are indicating these quantities for NGC 6905, which it was not possible to determine $T_e[\text{N II}]$.

concluded that $\log(f_{\text{shocks}}/f_{\text{star}}) > -1$ defines the zone of shock-dominated structures, while $\log(f_{\text{shocks}}/f_{\text{star}}) < -2$ encompasses the photoionization-dominated structures, and the transition between the two, $-2 < \log(f_{\text{shocks}}/f_{\text{star}}) < -1$, is where both mechanisms are present. Given the (generally uncertain) parameters entering this ratio, a deeper understanding of it is in place, before further dedicated analyses.

The ionizing photon flux, f_{shocks} , is determined from the total radiative flux, $F_{\text{shocks}} = 2.28 \times 10^{-3} (V_{\text{shock}}/100 \text{ km s}^{-1})^3 (N_e/\text{cm}^{-3}) \text{ ergs cm}^{-2} \text{ s}^{-1}$, where V_{shock} is the shock velocity and N_e is the density of the pre-shocked gas (Dopita & Sutherland 1996), divided by the average energy of a photon emitted from the central star (L/S_*). Thus, the equation becomes $f_{\text{shocks}}/f_{\text{star}} = 9.12 \times 10^{-3} (V_{\text{shock}}/100 \text{ km s}^{-1})^3 (N_e/\text{cm}^{-3}) (\pi d^2/L)$, where d is the LISs’ distance from the central star (in cm) and L is the luminosity of the central star (in erg s^{-1}) (Lago et al. 2019). The issue here is that the usually uncertain distances to PNE ($\propto d^2$), the unknown density of pre-shocked gas ($\propto N_{\text{pre-shock}}$) and the exact velocity of the shock wave ($\propto V_{\text{shock}}^3$) prevent a unequivocal determination of the $f_{\text{shocks}}/f_{\text{star}}$ ratio. The explicit contribution of these parameters is as below.

(i) *Distances* - The distances of the PNE in our sample were mainly adopted from Frew et al. (2016); Guerrero et al. (2020b), otherwise additional references are quoted.

(ii) *Pre-shock density* - Because there is very little known about the

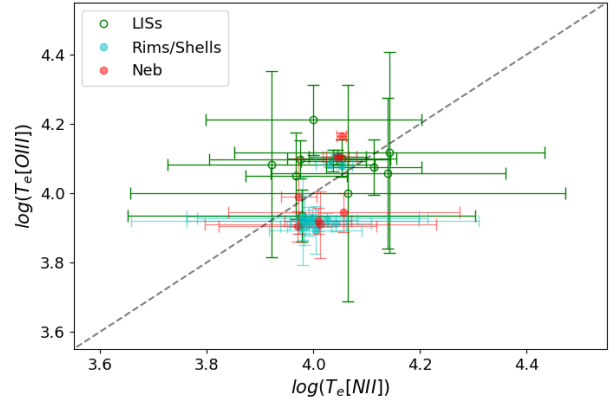


Figure 11. $T_e[\text{N II}]$ versus $T_e[\text{O III}]$ for all the components in our PNE’s sample. The dashed gray line represents the identity.

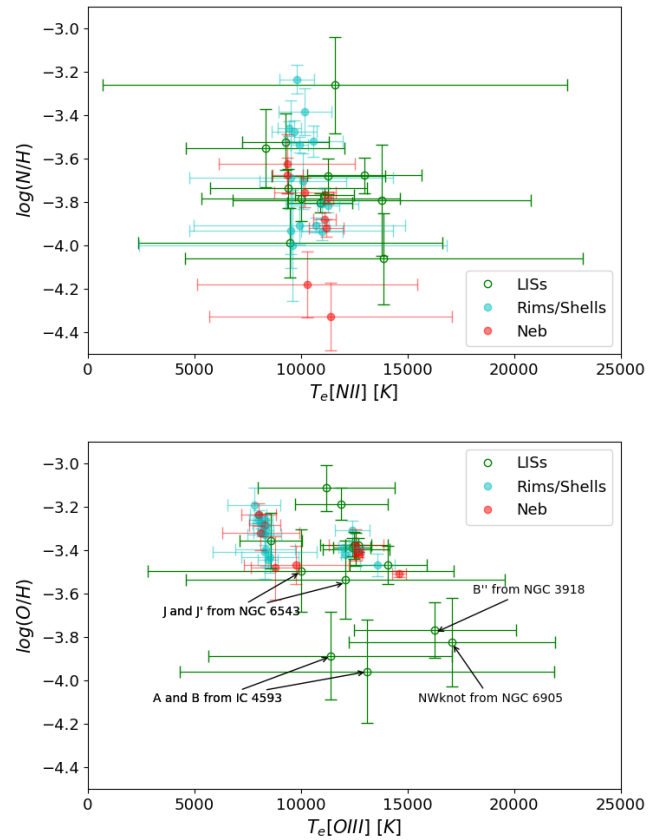


Figure 12. Variation of oxygen and nitrogen abundances as a function of electronic temperature. *Upper panel:* $T_e[\text{N II}]$ versus $\log(\text{N}/\text{H})$, in which there is no tendency considering the errors. *Lower panel:* $T_e[\text{O III}]$ versus $\log(\text{O}/\text{H})$. Arrows are indicating the position of the LISs having lower O/H than the rest of the points (see text).

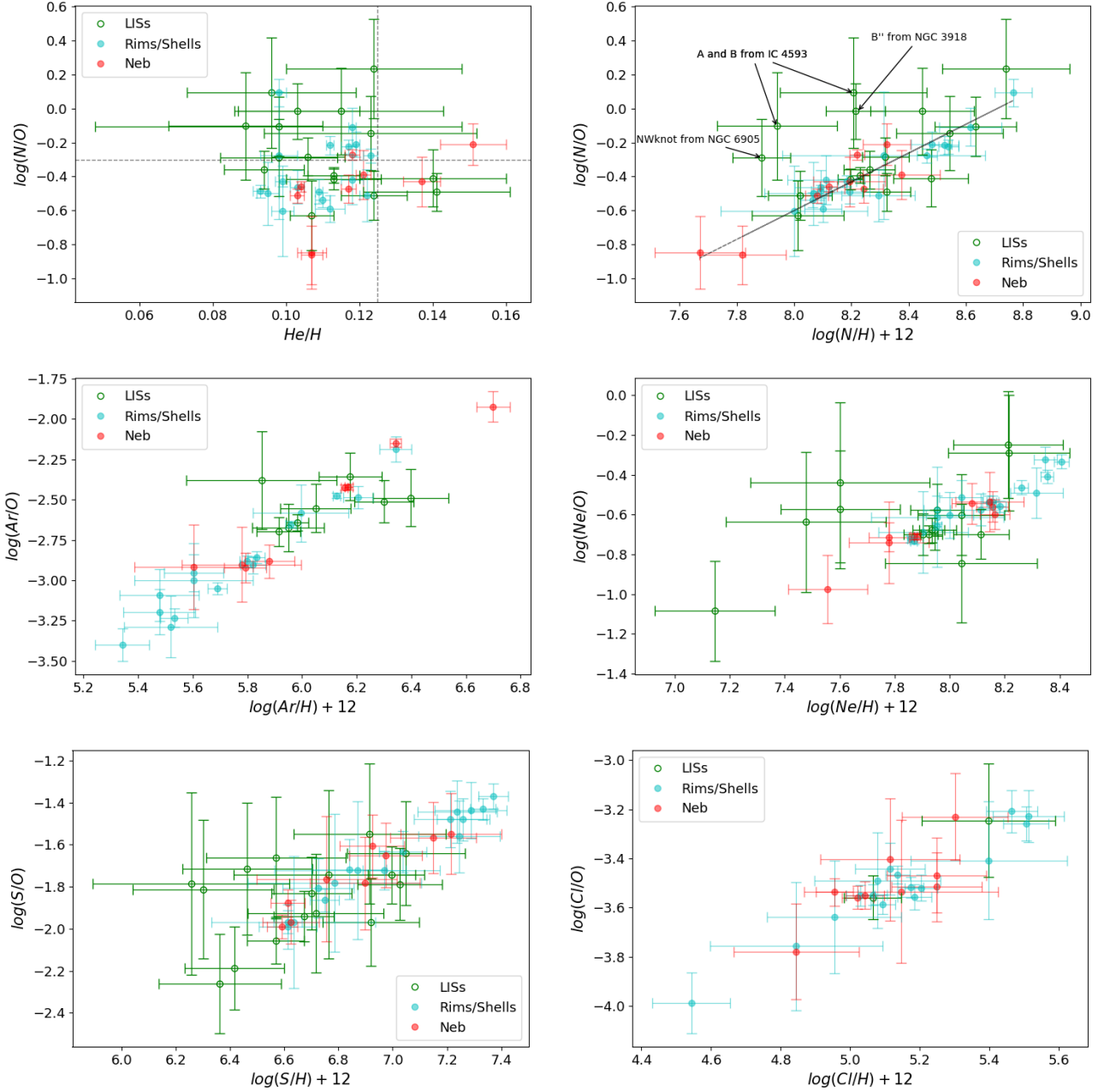


Figure 13. *Upper panels:* N/O abundance ratio plotted against He abundance (left) for our PN sample. The dashed lines are delimiting the criteria giving by Peimbert (1978) to define Type I PNe. In the right panel, $\log(N/O)$ versus $\log(N/H)+12$, where the dashed line is representing the best linear fit to our data (see text). *Middle panels:* relationship between Ar/O (Ne/O) abundance ratio and the total Ar (Ne) abundance on the left (right). *Lower panels:* relationship between S/O (Cl/O) abundance ratio and the total S (Cl) abundance on the left (right).

pre-shock density, the $f_{\text{shocks}}/f_{\text{star}}$ ratio is determined for a range of $N_{\text{pre-shock}}$ from 0.1 to 10000 cm^{-3} . We also point out that the density of the post-shocked gas (LISs) and pre-shocked gas (surrounding gas) are dependent parameters. At the shock jump, contact discontinuity, we get $N_{\text{post-shock}} = ((\gamma+1)M^2)/((\gamma-1)M^2+2) \times N_{\text{pre-shock}}$ (see e.g. Mellema 2004), where γ is the adiabatic index (5/3 for an ideal gas) and M is the Mach number of the shock wave, defined as $V_{\text{shock}}/V_{\text{sound}}$, where V_{sound} is the sound speed in the pre-shocked gas and its value is $\sim 12\text{--}15 \text{ km s}^{-1}$ for a gas with $T \sim 10000 \text{ K}$. For the case of a strong shock ($M \gg 1$) and ideal monoatomic gas, $N_{\text{post-shock}} \approx 4 \times N_{\text{pre-shock}}$. The post-shocked

gas becomes less dense for lower Mach numbers (or V_{shock}). In particular $V_{\text{shock}} > 45 \text{ km s}^{-1}$ yields $N_{\text{post-shock}}/N_{\text{pre-shock}} > 3$, and $25 < V_{\text{shock}} < 45 \text{ km s}^{-1}$ yields $N_{\text{post-shock}}/N_{\text{pre-shock}} > 2$ (for $V_{\text{sound}} = 15 \text{ km s}^{-1}$). Therefore, $f_{\text{shocks}}/f_{\text{star}}$ ratio is computed considering a $N_{\text{pre-shock}}$ that is consistent with the observed $N_{\text{post-shock}}$ of LISs.

(iii) *Inclination* - The limited information about the inclination of PNe and LISs does not allow for a direct determination of the expansion velocities. Hence, to derive the $f_{\text{shocks}}/f_{\text{star}}$ ratio a range of velocities, 20 to 140 km s^{-1} , with steps of 20 km s^{-1} , is considered. The radial velocities were adopted from Guerrero et al. (2020b) and Cuesta et al.

(1993), and they are illustrated in Fig. 14 as lower limits (vertical dashed lines).

In an attempt of applying these ideas to the LISs of each PN in our sample, Fig. 14 displays the $\log(f_{\text{shocks}}/f_{\text{star}})$ ratio as function of the expansion velocity, for different distances from the central star (circle, triangle and square points) and various pre-shock densities (colour-bars).

- IC 4593 (top-left panel): The very small radial velocity of the LISs ($1\text{--}2\text{ km s}^{-1}$) suggests a highly inclined nebula, which gives a expansion velocity up to 100 km s^{-1} . These LISs have N_e of $\sim 2000\text{--}3000\text{ cm}^{-3}$ corresponding to $N_{\text{pre-shock}}$ of $\sim 500\text{--}750\text{ cm}^{-3}$. We argue that shock interaction becomes important for $V_{\text{exp}} > 60\text{ km s}^{-1}$. Lower pre-shock densities would require higher shock velocities. The minimum inclination angle with respect to the light of sight, for an expansion velocity of 60 km s^{-1} is $\sim 88^\circ$. The contribution of shocks in the excitation of the LISs of IC 4593 is as likely as that of pure photo-ionization processes.

- Hen 2-186 (top-right panel): This nebula shows the fastest LISs in our sample, with $V_{\text{exp}} \geq 135\text{ km s}^{-1}$. Such a high velocity is very likely responsible for shocked-heated gas. We get $-1 < \log(f_{\text{shocks}}/f_{\text{star}}) < -2$ (in the transition zone), for $2 < \log(N_{\text{pre-shock}}) < 3$, and higher ratios for higher densities. $N_{\text{pre-shock}} \sim 250\text{--}450\text{ cm}^{-3}$ are implied from the LISs electron densities, $\sim 1000\text{--}1700\text{ cm}^{-3}$. There is strong indication for a non-negligible contribution of shocks for the LISs of Hen 2-186.

- Hen 2-429 (middle-left panel): LISs embedded in this nebula have N_e in the range of $\sim 3000\text{--}4000\text{ cm}^{-3}$, which corresponds to $\log(N_{\text{pre-shock}})$ between 2.8 and 3.0. The radial velocity of the LISs is 5.9 km s^{-1} . Only $V_{\text{exp}} \geq 40\text{ km s}^{-1}$ (inclination angle of $\sim 81^\circ\text{--}82^\circ$ respect to the light of sight) would be indicative of significant shocks contribution, even though, shock-excitation in the spectrum of the LISs of Hen 2-429 cannot be ruled out.

- NGC 3918 (middle-right panel): An electron density of $\sim 1500\text{--}2000\text{ cm}^{-3}$ has been estimated for its LISs that correspond to $N_{\text{pre-shock}} \sim 400\text{--}500\text{ cm}^{-3}$, depending on the Mach number. For such pre-shock densities only $V_{\text{exp}} > 40\text{ km s}^{-1}$ yield to a non-negligible contribution of shocks, at a distance from the central star of $6 \times 10^{-17}\text{ cm}$ (square symbols). The radial velocities of the LISs in NGC 3918 are 27 km s^{-1} (A) and 10 km s^{-1} (B). The excitation of both LISs can be attributed to shocks if $V_{\text{exp}} > 60\text{ km s}^{-1}$, or equivalently, their inclination angles respect to the light of sight are at least of 63° and 80° , respectively.

- NGC 6543 (bottom-left panel): In this nebula the LISs are characterized by $N_e \sim 950\text{--}1000\text{ cm}^{-3}$, or equivalently $N_{\text{pre-shock}} \sim 250\text{ cm}^{-3}$. Their radial velocity is 39 km s^{-1} (Miranda & Solf 1992; Reed et al. 1999; Guerrero et al. 2020b). A distance of 1.2 kpc (Gómez-Gordillo et al. 2020) to NGC 6543 is considered. The contribution of shocks becomes noteworthy for $V_{\text{exp}} > 60\text{ km s}^{-1}$. The morpho-kinematic analysis of NGC 6543 gives an inclination angle of $\sim 55^\circ$ (Miranda & Solf 1992) implying a de-projected expansion velocity of $\sim 68\text{ km s}^{-1}$. The LISs excitation ratio in NGC 6543 is very likely between -2 and -1 , in the transition zone, and therefore shock contribution cannot be ruled out.

- NGC 6905 (bottom-right panel): It is characterized by very low LIS' N_e , between 200 and 300 cm^{-3} , or $N_{\text{pre-shock}} \sim 55\text{--}70\text{ cm}^{-3} \approx 100\text{ cm}^{-3}$. The radial velocity of the PN and LIS are 30 and 50 km s^{-1} , respectively. For such low $N_{\text{pre-shock}}$, we obtain ratios greater than -2 , for V_{exp} between 60 and 80 km s^{-1} , or inclination angles of $45^\circ\text{--}65^\circ$ with respect to the light of sight. Both mechanisms, photo-

ionization and shock-heating likely contribute to the LISs' excitation in this PN.

Overall, taking into account the radial velocities, the LISs distances to the central stars, as well as the pre- and post-shock densities, we conclude that shock contribution cannot be ruled out as a possible excitation mechanism for most of the LISs in our sample. However, only the LISs in Hen 2-186, with radial velocity of 135 km s^{-1} , unequivocally lie in the shock-dominated zone. We also note that pre-shock densities lower than 100 cm^{-3} result in negligible shock contribution and $\log(f_{\text{shocks}}/f_{\text{star}}) > -2$ for V_{exp} up to $100\text{--}120\text{ km s}^{-1}$.

Another commonly used way of investigating the photo- versus shock-excitation of astrophysical objects is through diagnostic diagrams such as Sabbadin, Minello & Bianchini (1977) or Riesgo & López (2006), which are based on line ratios sensitive to these excitation processes. In Paper I, we discussed these diagnostic tools, and given their relevance, our forthcoming work will analyse these and other diagnostic diagrams for a statistically significant sample of PNe that host low-ionization structures combined with predictions from photoionization and shock models.

6 CONCLUSIONS

The spectroscopic analysis of six PNe with embedded LISs was carried out. Physico-chemical properties of the PNe with different structural components were computed and compared with the results in the literature.

After analyzing the properties of the LISs and their host PNe, we reinforce the conclusions of previous works that the electron density of LISs are lower (or at most equal) than those of the PN main structures (rims and shells). Regarding electron temperatures, we point out a *possible* different trends between estimations based on the nitrogen or the oxygen diagnostic lines. $T_e[\text{N II}]$ does not exhibit significant variations throughout the components, whereas $T_e[\text{O III}]$ appears to take slightly higher values for LISs relative to rims and shells, but also with much higher uncertainties, therefore not allowing robust conclusions.

In terms of abundances, as on Paper I (and the previous ones in the series), we do not find any trend between components. We have to mention the lower O/H for a couple of LISs, which would thus imply a non-negligible variation. However, these LISs also have extremely uncertain (higher, sometimes exceeding 15000 K) $T_e[\text{O III}]$, which result in suspicious face values for their oxygen abundances.

In an attempt to better understand the excitation mechanisms present in LISs, the diagnostic diagram defined on Paper I – $\log(f_{\text{shocks}}/f_{\text{star}})$ – was used, together with LISs kinematics. Considering that there are uncertainties on distances, pre-shock densities and radial velocities, we argue that the contribution of shocks to the excitation appears to be non-negligible for the PNe in our sample. In particular, shocks seems to be unambiguously associated with Hen 2-186' LISs, while for the remaining PNe the dependence on the inclination angle is much stronger, and since PNe do not have preferential orientations, shock excitation is not mandatory.

It seems evident the need to increase the sample of LISs to be able to perform a statistical analysis that takes into account all the properties found in recent years for these poorly understood structures. That is why these six PNe with LISs, jointly with a compilation of those already published in previous works, will be analysed in a forthcoming work. For this purpose, a statistical approach will be followed

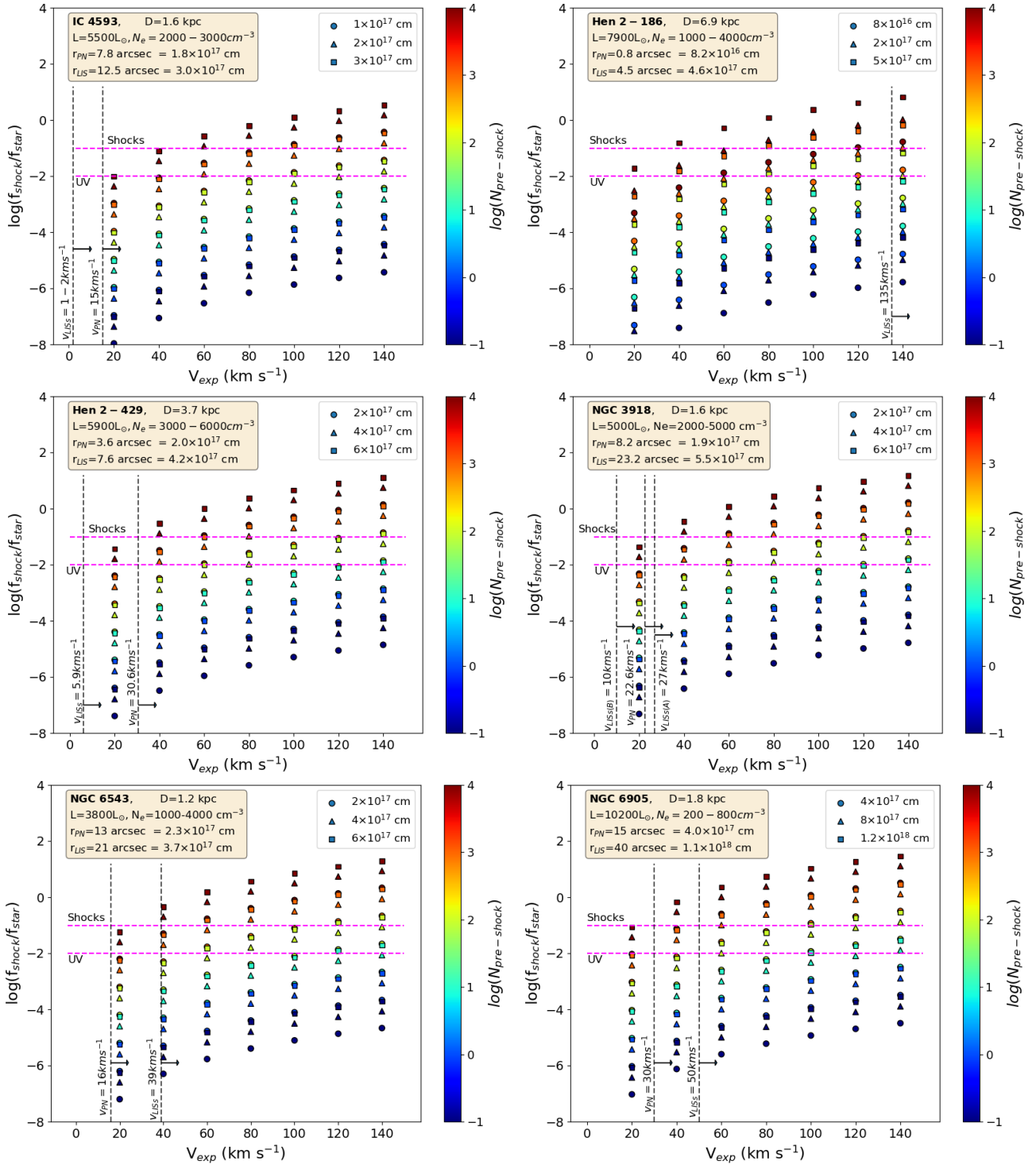


Figure 14. Variation of the $\log(f_{\text{shocks}}/f_{\text{star}})$ ratio as a function of the shock velocity, for three distance from the central stars (circle, triangle and square symbols), and a range of pre-shock densities from 0.1 up to 10000 cm⁻³ for each nebula of our sample. The velocities are taken from Guerrero et al. (2020b) for all PNe except NGC 6905 Cuesta et al. (1993). The parameters of the central stars are taken from Table 2. The vertical dashed-line indicate the projected spectroscopic velocities of the LIS and host PNe. The horizontal arrows denote the lower limit of the observed velocities. The horizontal dashed-lines indicate the limits of the photo-ionization and shock dominated regions defined by Akras & Gonçalves (2016).

to derive the distribution of physical, chemical and main excitation mechanism of the low-ionization structures in planetary nebulae.

ACKNOWLEDGEMENTS

We would like to thank Martín Guerrero, the referee, for his constructive comments and suggestions that helped to improve this work. This paper contains data taken jointly with A. Mampaso and R. Corradi, back in 2001, during a wonderful week of observations at the Roque de los Muchachos. We are also as much as thankful to H. Schwarz (in memoriam), the observer of the Danish data. This research is supported by a PhD grant from CAPES – the Brazilian Federal Agency for Support and Evaluation of Graduate Education within the Education Ministry. DGR acknowledges the CNPq grants 428330/2018-5 and 313016/2020-8. SA thanks the support under the grant 5077 financed by IAASARS/NOA.

DATA AVAILABILITY

Some of the spectroscopic data underlying this article are available at the [Isaac Newton Group Archive](#).

REFERENCES

- Acker A., Jasiewicz G., Koepfen J., Stenholm B., 1989, *A&AS*, **80**, 201
- Akashi M., Soker N., 2008, *MNRAS*, **391**, 1063
- Akras S., Gonçalves D. R., 2016, *MNRAS*, **455**, 930
- Akras S., López J. A., 2012, *MNRAS*, **425**, 2197
- Akras S., Gonçalves D. R., Ramos-Larios G., 2017, *MNRAS*, **465**, 1289
- Akras S., Monteiro H., Aleman I., Farias M. A. F., May D., Pereira C. B., 2020a, *MNRAS*, **493**, 2238
- Akras S., Gonçalves D. R., Ramos-Larios G., Aleman I., 2020b, *MNRAS*, **493**, 3800
- Akras S., et al., 2022, *MNRAS*, **512**, 2202
- Ali A., Dopita M. A., 2017, *Publ. Astron. Soc. Australia*, **34**, e036
- Aller L. H., 1968, in Osterbrock D. E., O'dell C. R., eds, Vol. 34, *Planetary Nebulae*. p. 339
- Balick B., 1987, *AJ*, **94**, 671
- Balick B., Frank A., 2002, *ARA&A*, **40**, 439
- Balick B., Bignell C. R., Hjellming R. M., Owen R., 1987, *AJ*, **94**, 948
- Balick B., Rugers M., Terzian Y., Chengalur J. N., 1993, *ApJ*, **411**, 778
- Balick B., Perinotto M., Maccioni A., Terzian Y., Hajian A., 1994, *ApJ*, **424**, 800
- Balick B., Alexander J., Hajian A. R., Terzian Y., Perinotto M., Patriarchi P., 1998, *AJ*, **116**, 360
- Balick B., Frank A., Liu B., 2019, *ApJ*, **877**, 30
- Balick B., Frank A., Liu B., 2020, *ApJ*, **889**, 13
- Barker T., 1978a, *ApJ*, **219**, 914
- Barker T., 1978b, *ApJ*, **220**, 193
- Benjamin R. A., Skillman E. D., Smits D. P., 1999, *ApJ*, **514**, 307
- Bohigas J., Olguín L., 1996, *Rev. Mex. Astron. Astrofis.*, **32**, 47
- Cahn J. H., 1976, *AJ*, **81**, 407
- Cavichia O., Costa R. D. D., Maciel W. J., 2010, *Rev. Mex. Astron. Astrofis.*, **46**, 159
- Clegg R. E. S., Harrington J. P., Barlow M. J., Walsh J. R., 1987, *ApJ*, **314**, 551
- Corradi R. L. M., Manso R., Mampaso A., Schwarz H. E., 1996, *A&A*, **313**, 913
- Corradi R. L. M., Guerrero M., Manchado A., Mampaso A., 1997, *New Astron.*, **2**, 461
- Corradi R. L. M., Perinotto M., Villaver E., Mampaso A., Gonçalves D. R., 1999, *ApJ*, **523**, 721
- Corradi R. L. M., Gonçalves D. R., Villaver E., Mampaso A., Perinotto M., Schwarz H. E., Zanin C., 2000a, *ApJ*, **535**, 823
- Corradi R. L. M., Gonçalves D. R., Villaver E., Mampaso A., Perinotto M., 2000b, *ApJ*, **542**, 861
- Corradi R. L. M., Schönberner D., Steffen M., Perinotto M., 2003, *MNRAS*, **340**, 417
- Costa R. D. D., Chiappini C., Maciel W. J., de Freitas Pacheco J. A., 1996, *A&AS*, **116**, 249
- Cuesta L., Phillips J. P., Mampaso A., 1993, *A&A*, **267**, 199
- Danehar A., Parker Q. A., Steffen W., 2016, *AJ*, **151**, 38
- De Araújo F. X., Marcolino W. L. F., Pereira C. B., Cuisinier F., 2002, *AJ*, **124**, 464
- Delgado Inglada G., Rodríguez M., Mampaso A., Viironen K., 2009, *ApJ*, **694**, 1335
- Delgado-Inglada G., Morisset C., Stasińska G., 2014, *MNRAS*, **440**, 536
- Derlopa S., Akras S., Boumis P., Steffen W., 2019, *MNRAS*, **484**, 3746
- Dopita M. A., Sutherland R. S., 1996, *ApJS*, **102**, 161
- Dyson J. E., Hartquist T. W., Pettini M., Smith L. J., 1989, *MNRAS*, **241**, 625
- Ercolano B., Morisset C., Barlow M. J., Storey P. J., Liu X. W., 2003, *MNRAS*, **340**, 1153
- Fang X., Guerrero M. A., Miranda L. F., Riera A., Velázquez P. F., Raga A. C., 2015, *MNRAS*, **452**, 2445
- Fang X., Zhang Y., Kwok S., Hsia C.-H., Chau W., Ramos-Larios G., Guerrero M. A., 2018, *ApJ*, **859**, 92
- Filippenko A. V., 1982, *PASP*, **94**, 715
- Frew D. J., Parker Q. A., Bojičić I. S., 2016, *MNRAS*, **455**, 1459
- García-Díaz M. T., López J. A., Steffen W., Richer M. G., 2012, *ApJ*, **761**, 172
- García-Rojas J., Peña M., Morisset C., Delgado-Inglada G., Mesa-Delgado A., Ruiz M. T., 2013, *A&A*, **558**, A122
- García-Rojas J., Madonna S., Luridiana V., Sterling N. C., Morisset C., Delgado-Inglada G., Toribio San Cipriano L., 2015, *MNRAS*, **452**, 2606
- García-Segura G., López J. A., Steffen W., Meaburn J., Manchado A., 2006, *ApJ*, **646**, L61
- García-Segura G., Ricker P. M., Taam R. E., 2018, *ApJ*, **860**, 19
- García-Segura G., Taam R. E., Ricker P. M., 2020, *ApJ*, **893**, 150
- García-Segura G., Taam R. E., Ricker P. M., 2021, *ApJ*, **914**, 111
- Giammanco C., et al., 2011, *A&A*, **525**, A58
- Girard P., Köppen J., Acker A., 2007, *A&A*, **463**, 265
- Gómez-González V. M. A., et al., 2022, *MNRAS*, **509**, 974
- Gómez-Gordillo S., Akras S., Gonçalves D. R., Steffen W., 2020, *MNRAS*, **492**, 4097
- Gonçalves D. R., Corradi R. L. M., Mampaso A., 2001, *ApJ*, **547**, 302
- Gonçalves D. R., Corradi R. L. M., Mampaso A., Perinotto M., 2003, *ApJ*, **597**, 975
- Gonçalves D. R., Mampaso A., Corradi R. L. M., Perinotto M., Riera A., López-Martín L., 2004, *MNRAS*, **355**, 37
- Gonçalves D. R., Ercolano B., Carnero A., Mampaso A., Corradi R. L. M., 2006, *MNRAS*, **365**, 1039
- Gonçalves D. R., Mampaso A., Corradi R. L. M., Quireza C., 2009, *MNRAS*, **398**, 2166
- Górny S. K., 2014, *A&A*, **570**, A26
- Górny S. K., Tyenda R., 2000, *A&A*, **362**, 1008
- Górny S. K., Schwarz H. E., Corradi R. L. M., Van Winckel H., 1999, *A&AS*, **136**, 145
- Gruenwald R., Viegas S. M., 1998, *ApJ*, **501**, 221
- Guerrero M. A., Vázquez R., López J. A., 1999, *AJ*, **117**, 967
- Guerrero M. A., Ramos-Larios G., Toalá J. A., Balick B., Sabin L., 2020a, *MNRAS*, **495**, 2234
- Guerrero M. A., Suzett Rechy-García J., Ortiz R., 2020b, *ApJ*, **890**, 50
- Hajian A. R., Balick B., Terzian Y., Perinotto M., 1997, *ApJ*, **487**, 304
- Henry R. B. C., Kwitter K. B., Balick B., 2004, *AJ*, **127**, 2284
- Henry R. B. C., Stephenson B. G., Miller Bertolami M. M., Kwitter K. B., Balick B., 2018, *MNRAS*, **473**, 241
- Howarth I. D., 1983, *MNRAS*, **203**, 301
- Hyung S., Aller L. H., Feibelman W. A., Lee W. B., de Koter A., 2000, *MNRAS*, **318**, 77
- Kaler J. B., 1970, *ApJ*, **160**, 887

- Kaler J. B., 1978, *ApJ*, **225**, 527
- Kaler J. B., 1986, *ApJ*, **308**, 322
- Kingsburgh R. L., Barlow M. J., 1994, *MNRAS*, **271**, 257
- Kwitter K. B., Henry R. B. C., 1998, *ApJ*, **493**, 247
- Kwitter K. B., Henry R. B. C., Milingo J. B., 2003, *PASP*, **115**, 80
- Lago P. J. A., Costa R. D. D., Faúndez-Abans M., Maciel W. J., 2019, *MNRAS*, **489**, 2923
- Lopez J. A., Vazquez R., Rodriguez L. F., 1995, *ApJ*, **455**, L63
- Manchado A., Guerrero M. A., Stanghellini L., Serra-Ricart M., 1996, The IAC morphological catalog of northern Galactic planetary nebulae. -
- Manchado A., Stanghellini L., Villaver E., García-Segura G., Shaw R. A., García-Hernández D. A., 2015, *ApJ*, **808**, 115
- Mari M. B., Gonçalves D. R., Akras S., 2020, *Galaxies*, **8**, 46
- Marquez-Lugo R. A., Ramos-Larios G., Guerrero M. A., Vázquez R., 2013, *MNRAS*, **429**, 973
- Matsuura M., et al., 2009, *ApJ*, **700**, 1067
- Medina S., Peña M., Morisset C., Stasińska G., 2006, *Rev. Mex. Astron. Astrofis.*, **42**, 53
- Mellema G., 2004, *A&A*, **416**, 623
- Miranda L. F., Solf J., 1992, *A&A*, **260**, 397
- Miranda L. F., et al., 2021, arXiv e-prints, p. [arXiv:2105.05186](https://arxiv.org/abs/2105.05186)
- Miszalski B., Acker A., Parker Q. A., Moffat A. F. J., 2009, *A&A*, **505**, 249
- Monreal-Ibero A., Walsh J. R., 2020, *A&A*, **634**, A47
- Montoro-Molina B., Guerrero M. A., Pérez-Díaz B., Toalá J. A., Cazzoli S., Miller Bertolami M. M., Morisset C., 2022, *MNRAS*, **512**, 4003
- Osterbrock D. E., Ferland G. J., 2006, *Astrophysics of gaseous nebulae and active galactic nuclei*. -
- Peña M., Ruiz-Escobedo F., Rechy-García J. S., García-Rojas J., 2017, *MNRAS*, **472**, 1182
- Peimbert M., 1978, in Terzian Y., ed., Vol. 76, *Planetary Nebulae*. pp 215–224
- Pena M., Torres-Peimbert S., 1985, *Rev. Mex. Astron. Astrofis.*, **11**, 35
- Pena M., Stasińska G., Esteban C., Koesterke L., Medina S., Kingsburgh R., 1998, *A&A*, **337**, 866
- Perinotto M., 1991, *ApJS*, **76**, 687
- Perinotto M., 2000, *Ap&SS*, **274**, 205
- Perinotto M., Bencini C. G., Pasquali A., Manchado A., Rodríguez Espinosa J. M., Stanga R., 1999, *A&A*, **347**, 967
- Perinotto M., Morbidelli L., Scatarzi A., 2004, *MNRAS*, **349**, 793
- Phillips J. P., 1998, *A&A*, **340**, 527
- Ramos-Larios G., Santamaría E., Guerrero M. A., Marquez-Lugo R. A., Sabin L., Toalá J. A., 2016, *MNRAS*, **462**, 610
- Ramos-Larios G., Guerrero M. A., Sabin L., Santamaría E., 2017, *MNRAS*, **470**, 3707
- Reay N. K., Walton N. A., Atherton P. D., 1988, *MNRAS*, **232**, 615
- Reed D. S., Balick B., Hajian A. R., Klayton T. L., Giovanardi S., Casertano S., Panagia N., Terzian Y., 1999, *AJ*, **118**, 2430
- Richer M. G., McCall M. L., Martin P. G., 1991, *ApJ*, **377**, 210
- Riesgo H., López J. A., 2006, *Rev. Mex. Astron. Astrofis.*, **42**, 47
- Robertson-Tessi M., Garnett D. R., 2005, *ApJS*, **157**, 371
- Sabbadin F., Minello S., Bianchini A., 1977, *A&A*, **60**, 147
- Schwarz H. E., Corradi R. L. M., Melnick J., 1992, *A&AS*, **96**, 23
- Soker N., 1998, *MNRAS*, **299**, 562
- Stanghellini L., Kaler J. B., 1989, *ApJ*, **343**, 811
- Stanghellini L., Kaler J. B., Shaw R. A., di Serego Alighieri S., 1995, *A&A*, **302**, 211
- Stanghellini L., Guerrero M. A., Cunha K., Manchado A., Villaver E., 2006, *ApJ*, **651**, 898
- Steffen W., López J. A., Lim A., 2001, *ApJ*, **556**, 823
- Tsamis Y. G., Barlow M. J., Liu X. W., Danziger I. J., Storey P. J., 2003, *MNRAS*, **345**, 186
- Tylenda R., Acker A., Stenholm B., Koeppen J., 1992, *A&AS*, **95**, 337
- Ventura P., Stanghellini L., Dell’Aglì F., García-Hernández D. A., 2017, *MNRAS*, **471**, 4648
- Vorontsov-Vel’Yaminov B. A., 1961, *Soviet Ast.*, **5**, 186
- Walsh J. R., Monreal-Ibero A., Barlow M. J., Ueta T., Wesson R., Zijlstra A. A., 2016, *A&A*, **588**, A106
- Walsh J. R., et al., 2018, *A&A*, **620**, A169
- Weidmann W. A., et al., 2020, *A&A*, **640**, A10
- Wesson R., Liu X. W., 2004, *MNRAS*, **351**, 1026
- Wesson R., Stock D. J., Scicluna P., 2012, *MNRAS*, **422**, 3516
- Williams R., Jenkins E. B., Baldwin J. A., Zhang Y., Sharpee B., Pellegrini E., Phillips M., 2008, *ApJ*, **677**, 1100

APPENDIX A: FLUX LINES TOGETHER WITH IONIC AND TOTAL ABUNDANCES

The flux emission lines measurements and obtained results are present in this section. The fluxes were corrected for interstellar reddening and then they were used to estimate T_e , N_e , ionic and total abundances for all nebulae present in this paper together with the smaller structures as rims, shells and LISs.

Table A1: IC 4593

Line	Ion	PA=62				PA=139				
		NE shell 5px-3.5"	Neb 22px-15"	SW Shell 5px-3.5"	C 3px-2.1"	A 5px-3.5"	SE Shell 9px-6.3"	Neb 22px-15"	NW Shell 9px-6.3"	B 5px-3.5"
3727.00	[O II]b	55±1	45±1	54±2	126±4	151±17	42±2	44±4	38±6	74±8
3868.75	[Ne III]	28.3±0.4	33.3±0.8	23.2±0.9	22.7±1.7	31.5±10.3	25.9±0.6	30.8±1.3	20.0±1.1	23.4±7.3
3889.05	H I+He I	20.4±0.3	14.3±0.8	19.2±0.8	21.2±1.3	24.5±12.3	18.0±0.5	17.7±1.1	16.1±1.7	18.8±6.6
3967.46	[Ne III]	9.4±0.4	5.1±0.9	5.9±0.8	6.4±1.4	8.8±7.6	5.9±0.3	7.2±0.9	2.2±1.4	3.8±3.4
3970.07	H I	16.8±0.4	16.2±0.9	16.2±0.8	15.8±1.5	17.0±7.8	17.6±0.3	16.2±0.9	16.5±1.4	17.3±6.3
4101.74	H I	27.1±0.4	22.8±0.6	25.2±0.8	26.5±1.3	33.1±10.4	25.4±0.3	23.2±0.7	28.5±1.2	27.2±6.9
4340.47	H I	47.8±0.3	44.6±0.7	44.6±0.6	45.7±1.1	51.7±8.1	45.1±0.8	45.3±0.5	48.4±1.3	50.6±3.9
4363.21	[O III]	1.8±0.1	1.8±0.4	1.9±0.3	2.2±0.6	6.0±4.3	1.8±0.3	2.3±0.3	1.7±0.5	4.3±2.5
4471.50	He I	5.3±0.2	5.0±0.5	5.2±0.4	5.3±0.9	-	5.2±0.4	4.8±0.3	4.0±0.7	-
4685.68	He II	-	2.0±0.4	-	-	-	-	2.8±0.3	-	-
4711.37	[Ar IV]	0.6±0.1	0.8±0.3	0.5±0.2	-	-	0.6±0.3	0.8±0.2	-	-
4861.33	H I	100	100	100	100	100	100	100	100	100
4958.91	[O III]	173±1	192±1	177±1	183±2	149±10	167±1	183±1	168±2	150±10
5006.84	[O III]	517±3	569±3	523±5	528±8	415±33	534±1	542±3	505±3	431±14
5517.66	[Cl III]	0.4±0.1	0.4±0.2	0.5±0.1	0.7±0.3	-	0.2±0.1	0.5±0.4	0.3±0.2	-
5537.60	[Cl III]	0.4±0.1	0.4±0.2	0.4±0.2	0.9±0.4	-	0.2±0.1	0.5±0.4	0.3±0.2	-
5754.60	[N II]	0.2±0.1	0.2±0.1	0.2±0.1	0.4±0.3	3.0±1.8	0.12±0.09	0.2±0.1	0.2±0.1	1.9±1.0
5875.66	He I	15.7±0.1	15.8±0.3	12.7±0.2	17.0±0.6	15.4±2.7	15.2±0.3	15.5±0.3	15.8±0.5	14.6±2.9
6300.30	[O I]	-	-	0.15±0.08	0.4±0.2	4.4±1.8	-	-	-	4.2±1.8
6312.10	[S III]	0.8±0.1	0.7±0.2	0.8±0.1	0.9±0.3	-	0.4±0.1	0.8±0.2	0.8±0.2	-
6548.10	[N II]	4.5±0.1	4.5±0.2	5.4±0.2	11.2±0.7	30.5±1.9	2.9±0.1	4.2±0.1	5.4±0.3	16.6±3.0
6562.77	H I	292±2	275±2	281±2	269±5	273±22	284±3	279±2	292±4	281±15
6583.50	[N II]	12.1±0.1	12.3±0.2	13.2±0.3	26.7±0.9	81.8±7.1	7.9±0.2	11.7±0.2	14.4±0.5	53.5±4.9
6678.16	He I	3.5±0.1	4.3±0.2	4.4±0.2	3.5±0.3	3.5±1.4	2.4±0.1	4.1±0.1	3.6±0.3	4.2±2.3
6716.44	[S II]	0.5±0.1	0.5±0.1	0.8±0.1	1.6±0.2	4.9±1.8	0.3±0.1	0.6±0.1	0.7±0.1	5.4±2.5
6730.82	[S II]	0.7±0.1	0.7±0.1	1.2±0.2	2.4±0.2	7.2±1.8	0.4±0.1	0.8±0.1	1.0±0.2	7.3±2.6
$\log F(H\beta)$		-12.30	-11.22	-11.74	-13.03	-13.85	-11.68	-11.22	-11.79	-13.55
$c(H\beta)$		0.13±0.01	0.05±0.01	0.06±0.01	0.02±0.02	0.14±0.09	0.22±0.01	0.05±0.01	0.12±0.02	0.16±0.08
Electron densities (cm^{-3}) and temperatures (K)										
N_e [S II]		2610±155	2840±626	2290±477	2360±355	2750±1222	2220±758	2810±545	2220±546	2100±1227
T_e [N II]		9950±4956	10300±5153	9550±4779	9510±7138	13900±9314	9630±7225	11400±5701	9550±4783	13800±6992
T_e [O III]		8470±472	8120±1805	8560±1353	8610±1465	13100±8770	8340±1390	8800±1148	8310±2445	11400±5710

Table A2: Ionic and total abundances of IC 4593.

Abundances	PA=62					PA=139				
	NE shell	Neb	SW Shell	C	A	SE Shell	Neb	NW Shell	B	
$10^2 \times \text{He}^+/\text{H}$	10.3±0.2	10.5±0.3	9.5±0.3	10.7±0.6	8.9±2.1	9.9±0.3	10.5±0.4	9.8±0.5	9.6±2.3	
$10^3 \times \text{He}^{2+}/\text{H}$	-	1.6±0.3	-	-	-	-	2.2±0.3	-	-	
$10^2 \times \text{He}/\text{H}$	10.3±0.2	10.7±0.3	9.5±0.3	10.7±0.6	8.9±2.1	9.9±0.3	10.7±0.4	9.8±0.5	9.6±2.3	
$10^6 \times \text{N}^+/\text{H}$	2.6±0.9	2.6±1.3	3.6±1.6	7.2±3.0	8.5±4.2	2.2±1.1	2.1±1.0	3.7±1.5	7.3±4.8	
icf(N)	47.7±25.0	25.0±18.0	32.6±22.2	14.1±9.1	9.4±7.9	44.8±37.5	22.4±15.5	56.2±41.1	29.7±27.5	
$10^5 \times \text{N}/\text{H}$	12.4±2.6	6.6±2.3	11.7±4.6	10.3±3.8	8.7±4.2	10.0±5.9	4.7±1.7	20.6±16.8	16.1±9.5	
$10^7 \times \text{O}^0/\text{H}$	-	-	3.0±2.0	7.7±5.0	25.6±8.8	-	-	-	25.9±17.4	
$10^5 \times \text{O}^+/\text{H}$	2.9±0.9	2.5±1.7	4.0±2.6	8.8±5.3	2.5±1.7	3.3±2.4	1.8±1.2	2.6±1.6	1.2±0.9	
$10^4 \times \text{O}^{2+}/\text{H}$	3.3±0.2	4.3±1.3	3.2±0.5	3.2±1.6	0.6±0.3	3.5±0.5	2.9±0.7	3.4±0.8	1.0±0.4	
icf(O)	1.00±0.00	1.01±0.01	1.00±0.00	1.00±0.00	1.00±0.00	1.00±0.00	1.01±0.01	1.00±0.00	1.00±0.00	
$10^4 \times \text{O}/\text{H}$	3.6±0.3	4.8±0.9	3.7±0.6	4.4±1.3	1.1±0.6	4.0±0.7	3.3±1.1	3.9±1.1	1.3±0.6	
$10^4 \times \text{Ne}^{2+}/\text{H}$	0.7±0.1	0.8±0.3	0.5±0.1	0.5±0.3	0.12±0.07	0.6±0.2	0.6±0.1	0.5±0.2	0.14±0.07	
icf(Ne)	1.6±0.2	1.6±0.3	1.8±0.9	2±1	3±1	1.6±0.3	1.07±0.07	1.6±0.2	1.8±0.4	
$10^4 \times \text{Ne}/\text{H}$	1.1±0.2	1.4±0.4	0.9±0.5	1.1±0.4	0.4±0.3	1.0±0.2	0.6±0.2	0.8±0.3	0.3±0.2	
$10^6 \times \text{Ar}^{2+}/\text{H}$	-	-	-	-	-	-	-	-	-	
$10^6 \times \text{Ar}^{3+}/\text{H}$	0.3±0.1	0.5±0.2	0.2±0.1	-	-	0.4±0.2	0.4±0.1	-	-	
$10^6 \times \text{Ar}^{4+}/\text{H}$	-	-	-	-	-	-	-	-	-	
icf(Ar) ⁽⁴⁾	1.08±0.06	1.07±0.04	1.11±0.26	1.00±0.00	1.00±0.00	1.08±0.65	1.07±0.18	1.00±0.00	1.00±0.00	
$10^6 \times \text{Ar}/\text{H}$	0.4±0.1	0.6±0.3	0.3±0.1	-	-	0.4±0.2	0.4±0.2	-	-	
$10^8 \times \text{S}^+/\text{H}$	3.7±1.3	4.1±2.2	7.7±3.4	14.7±6.1	20.0±10.3	2.8±1.4	3.9±1.9	6.3±2.7	20.8±11.8	
$10^6 \times \text{S}^{2+}/\text{H}$	4.3±0.5	4.6±2.3	4.0±0.8	4.2±1.8	1.3±1.1	2.5±0.8	3.3±1.3	4.3±1.7	1.3±0.7	
icf(S) ⁽⁴⁾	1.6±0.5	1.7±0.8	1.5±1.1	1.2±0.7	1.2±1.0	1.7±1.2	1.7±1.0	1.7±1.2	1.2±0.7	
$10^6 \times \text{S}/\text{H}$	6.9±2.2	7.9±3.7	6.1±4.5	5.2±3.0	1.8±1.5	4.3±3.0	5.7±3.4	7.4±5.2	2.0±1.2	
$10^7 \times \text{Cl}^{2+}/\text{H}$	0.8±0.2	1.1±0.6	0.9±0.3	1.8±0.7	-	0.5±0.3	1.0±0.6	0.6±0.3	-	
icf(Cl)	1.7±0.2	1.3±0.3	1.5±0.5	1.4±0.2	1.00±0.00	1.4±0.4	1.3±0.4	1.4±0.4	1.00±0.00	
$10^7 \times \text{Cl}/\text{H}$	1.3±0.3	1.4±0.9	1.2±0.5	2.5±1.1	-	0.7±0.4	1.3±0.6	0.9±0.4	-	

⁽⁴⁾ Calculated using Kingsburgh & Barlow (1994). When no S^{2+} is present, it was calculated using $\text{S}^{+2} = \text{S}^+ [4.677 + (\text{O}^{+2}/\text{O}^+)^{0.433}]$ from the same work.

Table A3: Hen 2-186.

Line	Ion	PA=29		
		A	Neb	B
3727.00	[O III]	5px-2"	1.3px-5.2"	5px-2"
3868.75	[Ne III]	346±55	127±4	302±39
3889.05	He I+He I	169±26	137±2	135±21
3968.43	[Ne III]	-	17.7±0.9	-
3970.07	H I	60±15	28±2	39±13
4101.74	H I	22±15	23±2	17±13
4340.47	H I	27±8	33±1	22±7
4363.21	[O III]	38.9±4.7	47.2±0.5	47.4±5.8
4471.50	He I	21.6±4.1	27.2±0.6	14.2±4.3
4685.68	He II	-	4.0±0.2	-
4711.37	[Ar IV]	58.5±4.3	57.5±0.5	46.4±5.2
4740.17	[Ar IV]	-	6.9±0.2	-
4861.33	H I	-	0.5±0.2	-
4958.91	[O III]	100	100	100
5006.84	[O III]	629±14	543±1	535±12
5517.66	[Cl III]	1980±50	1400±10	1530±60
5537.60	[Cl III]	-	0.6±0.1	-
5577.34	[O I]	-	1.0±0.1	-
5754.60	[N II]	-	0.4±0.1	-
5875.66	He I	10.0±2.1	4.9±0.1	5.1±1.4
6300.30	[O I]	15.8±2.6	12.4±0.2	14.9±1.9
6312.10	[S III]	30.1±4.0	16.9±0.3	34.1±3.1
6363.78	[O I]	5.7±2.5	4.1±0.1	3.3±2.3
6434.73	[Ar V]	11.3±2.2	5.9±0.2	9.7±2.4
6548.10	[N II]	2.8±1.9	1.5±0.1	-
6562.77	H I	119±8	73±1	137±10
6583.50	[N II]	274±13	283±2	279±16
6678.16	He I	355±23	222±1	395±26
6716.44	[S II]	2.1±1.5	3.4±0.1	4.0±1.8
6730.82	[S II]	21.6±2.7	10.3±0.3	28.1±3.0
7135.80	[Ar III]	27.6±2.9	17.3±0.2	32.3±3.1
$\log F(H\beta)$		18.6±3.0	20.1±0.3	18.7±2.7
$c(H\beta)$		-14.68	-12.58	-14.87
Electron densities (cm^{-3}) and temperatures (K)				
$N_e[S II]$		1710 ± 297	3990±125	1070±152
$N_e[Cl III]$		-	8070±1569	-
$N_e[Ar IV]$		-	5420±209	-
$T_e[N II]$		13000 ± 2684	11300±237	9280±2027
$T_e[O I]$		-	12700±3181	-
$T_e[O III]$		11900 ± 2177	14600±331	11200±3217

Table A4: Ionic and total abundances of Hen 2-186.

Abundances	PA=29	
	A	B
$10^3 \times \text{He}^+/\text{H}$	0.92±0.20	0.68±0.02
$10^2 \times \text{He}^{2+}/\text{H}$	4.9±0.4	5.02±0.04
$10^1 \times \text{He}/\text{H}$	1.41±0.20	1.18±0.02
$10^2 \times \text{N}^+/\text{H}$	3.9±0.8	3.3±0.2
icf(N)	5.4±1.6	4.9±0.5
$10^4 \times \text{N}/\text{H}$	2.1±0.4	1.6±0.1
$10^5 \times \text{O}^0/\text{H}$	2.3±0.7	1.9±0.2
$10^4 \times \text{O}^+/\text{H}$	1.0±0.3	0.53±0.08
$10^4 \times \text{O}^{2+}/\text{H}$	3.8±0.7	1.65±0.05
icf(O)	1.31±0.07	1.44±0.02
$10^4 \times \text{O}/\text{H}$	6.5±1.1	3.1±0.1
$10^5 \times \text{Ne}^{2+}/\text{H}$	9.8±2.3	3.9±0.1
icf(Ne)	1.31±0.08	1.45±0.02
$10^4 \times \text{Ne}/\text{H}$	1.3±0.3	0.6±0.1
$10^6 \times \text{Ar}^{2+}/\text{H}$	1.2±0.3	0.9±0.1
$10^7 \times \text{Ar}^{3+}/\text{H}$	-	7.3±0.3
$10^7 \times \text{Ar}^{4+}/\text{H}$	7.8±5.2	2.7±0.2
icf(Ar) ⁽⁵⁾	1.00±0.30	1.19±0.23
$10^6 \times \text{Ar}/\text{H}$	2.0±0.5	2.2±0.1
$10^7 \times \text{S}^+/\text{H}$	7.8±1.7	6.9±0.5
$10^6 \times \text{S}^{2+}/\text{H}$	6.8±3.1	2.5±0.1
icf(S) ⁽⁵⁾	1.4±0.5	1.3±0.2
$10^6 \times \text{S}/\text{H}$	10.6±3.8	4.1±0.6
$10^8 \times \text{Cl}^{2+}/\text{H}$	-	4.5±0.5
icf(Cl)	1.00±0.00	2.01±0.04
$10^8 \times \text{Cl}/\text{H}$	-	9.0±1.1

⁽⁵⁾ Calculated using [Kingsburgh & Barlow \(1994\)](#)

Table A5: Hen 2-429.

Line	Ion	PA=89	
		Neb	B ⁽⁶⁾
3727.00	[O II]b	15px-10.5"	5px-3.5"
3868.75	[Ne III]	121±12	347±129
3889.05	He I+He I	30±5	368±99
3968.43 ⁽⁷⁾	[Ne III]+H I	23±4	-
4101.74	H I	28±4	-
4340.47	H I	27±4	-
4363.21	[O III]	51±4	-
4471.50	He I	4±1	-
4685.68	He II	7±1	-
4861.33	H I	15±1	-
4958.91	[O III]	100	100
5006.84	[O III]	184±3	244±31
5517.66	[Cl III]	562±5	655±46
5537.60	[Cl III]	0.8±0.3	-
5754.60	[N II]	1.1±0.3	-
5875.66	He I	4.0±0.3	-
6300.30	[O I]	21.5±0.6	13.2±7.8
6312.10	[S III]	4.5±0.2	6.9±2.7
6363.78	[O I]	2.5±0.2	3.1±2.1
6548.10	[N II]	1.5±0.1	-
6562.77	H I	88±2	168±23
6583.50	[N II]	287±6	271±35
6678.16	He I	271 ±6	417±58
6716.44	[S II]	5.5±0.3	8.9±2.7
6730.82	[S II]	8.6±0.3	15.4±3.2
		16.0±0.5	24.8±4.1
		-13.04	-15.26
		2.12 ± 0.03	2.11 ± 0.19
			2.02±0.20
		Electron densities (cm ⁻³) and temperatures (K)	
		5710 ± 267	4310±1870
		5150 ± 2388	-
		9390 ± 723	-
		9790 ± 2449	-
		Stellar line fluxes from CSPN (erg/s/cm ²)	
		(3.19±0.49)×10 ⁻¹⁴	FWHM (Å)
		(7.51±1.40)×10 ⁻¹⁵	33±5
		(6.85±1.80)×10 ⁻¹⁵	36±8
		(1.40±0.04)×10 ⁻¹³	40±16
			38±1

⁽⁶⁾ A problem is detected in the H β line of this LIS, so the proposed solution was to use the F(H β) of the other LIS (A), therefore, the results found should be taken with caution.

⁽⁷⁾ Separation of these two emission lines was not possible in this case.

Table A6: Ionic and total abundances of Hen 2-429.

Abundances	PA=89	
	Neb	A ⁽⁹⁾
10 ¹ × He ⁺ /H	1.39±0.09	0.98±0.50
10 ² × He ²⁺ /H	1.21±0.09	-
10 ¹ × He/H	1.51±0.09	0.98±0.50
10 ² × N ⁺ /H	6.9±0.6	12.3±9.1
icf(N)	3.1±0.7	3.6±2.2
10 ⁴ × N/H	2.1±0.4	4.3±1.4
10 ⁵ × O ⁰ /H	1.0±0.1	5.0±1.4
10 ⁴ × O ⁺ /H	1.1±0.2	3.0±1.3
10 ⁴ × O ²⁺ /H	2.1±0.6	2.6±0.2
icf(O)	1.05±0.01	1.00±0.00
10 ⁴ × O/H	3.4±0.7	5.5±1.3
10 ⁵ × Ne ²⁺ /H	3.5±1.2	-
icf(Ne)	1.05±0.01	1.00±0.00
10 ⁵ × Ne/H	3.6±1.2	-
10 ⁷ × Ar ³⁺ /H	-	-
icf(Ar) ⁽¹⁰⁾	1.00±0.00	1.00±0.00
10 ⁷ × Ar/H	-	-
10 ⁶ × S ⁺ /H	1.2±0.1	1.3±0.4
10 ⁶ × S ²⁺ /H	6.4±2.2	8.6±5.8
icf(S) ⁽¹⁰⁾	1.1±0.3	1.0±0.2
10 ⁶ × S/H	8.4±2.3	9.9±2.0
10 ⁷ × Cl ²⁺ /H	1.4±0.9	-
icf(Cl)	1.39±0.02	1.00±0.00
10 ⁷ × Cl/H	2.0±0.7	-

⁽⁸⁾ Estimated using T_e for [N II] and [O III] from Neb

⁽⁹⁾ Estimated using T_e for [N II] and [O III] from Neb

⁽¹⁰⁾ Calculated using Kingsburgh & Barlow (1994). When no S⁺ is present, it was calculated using S²⁺ = S⁺ [4.677 + (O²⁺/O⁺)^{0.433}] from the same work.

Table A7: NGC 3918

Line	Ion	PA=30			PA=70			PA=40			PA=42		
		Neb	Rim	Rim1	Neb	Rim1	Rim2	B'	B	B''	A'	A	
3727.00	[O III]	76 ± 2	86 ± 2	82 ± 2	72 ± 2	64 ± 2	64 ± 2	118 ± 21	174 ± 20	89 ± 22	370 ± 15	222 ± 9	
3868.75	[Ne III]	122 ± 1	122 ± 2	147 ± 2	121 ± 2	126 ± 2	126 ± 2	156 ± 12	151 ± 12	59 ± 12	169 ± 11	162 ± 7	
3889.05	H I+He I	18.4 ± 0.5	16.9 ± 0.7	20.7 ± 0.7	18.9 ± 0.7	17.9 ± 0.5	17.9 ± 0.5	15.3 ± 4.3	29.8 ± 6.1	-	22.2 ± 3.5	22.5 ± 2.2	
3967.46	[Ne III]	33.8 ± 0.6	34.2 ± 1.0	40.5 ± 1.1	34.3 ± 0.9	36.6 ± 1.0	36.6 ± 1.0	65.6 ± 9.2	48.9 ± 6.8	-	43.4 ± 3.8	46.7 ± 3.1	
3970.07	H I	18.2 ± 0.6	18.3 ± 1.0	18.3 ± 1.0	18.0 ± 0.9	17.7 ± 1.0	17.7 ± 1.0	18.2 ± 9.3	17.7 ± 6.6	18.2 ± 8.4	18.7 ± 3.5	18.0 ± 3.2	
4101.74	H I	27.5 ± 0.5	24.8 ± 0.5	25.9 ± 0.6	26.9 ± 0.5	27.2 ± 0.6	27.2 ± 0.6	25.1 ± 3.9	26.4 ± 2.6	25.5 ± 6.0	24.7 ± 5.2	26.7 ± 1.0	
4267.15	C II	0.6 ± 0.2	-	0.6 ± 0.2	0.5 ± 0.2	0.5 ± 0.2	0.5 ± 0.2	-	-	-	-	-	
4340.47	H I	47.6 ± 0.4	45.4 ± 0.5	44.4 ± 0.5	45.9 ± 0.5	46.7 ± 0.5	46.7 ± 0.5	47.0 ± 3.6	47.5 ± 3.3	46.5 ± 6.4	43.3 ± 5.7	46.3 ± 1.3	
4363.21	[O III]	20.1 ± 0.3	17.9 ± 0.3	18.9 ± 0.4	20.1 ± 0.3	22.1 ± 0.4	22.1 ± 0.4	22.9 ± 2.8	23.0 ± 2.6	25.3 ± 5.8	18.3 ± 1.4	23.3 ± 1.1	
4471.50	He I	3.7 ± 0.2	4.6 ± 0.2	3.9 ± 0.2	3.3 ± 0.2	3.9 ± 0.2	3.9 ± 0.2	4.6 ± 1.5	4.9 ± 1.5	-	5.0 ± 1.2	4.5 ± 0.6	
4647.40	C III	6.3 ± 0.2	4.9 ± 0.2	1.8 ± 0.1	5.2 ± 0.1	6.2 ± 0.2	6.2 ± 0.2	-	-	-	-	-	
4685.68	He II	47.1 ± 0.4	19.9 ± 0.3	24.7 ± 0.3	48.9 ± 0.4	46.2 ± 0.4	46.2 ± 0.4	10.1 ± 1.8	22.6 ± 1.8	29.0 ± 4.3	14.8 ± 1.2	29.0 ± 0.9	
4711.37	[Ar IV]	7.6 ± 0.1	4.7 ± 0.2	4.7 ± 0.2	8.0 ± 0.2	8.5 ± 0.2	8.5 ± 0.2	4.9 ± 1.4	6.2 ± 1.3	5.6 ± 3.4	3.7 ± 0.7	5.4 ± 0.4	
4713.17	He I	0.5 ± 0.1	0.6 ± 0.2	0.5 ± 0.2	0.5 ± 0.2	0.5 ± 0.2	0.5 ± 0.2	-	-	-	-	0.6 ± 0.4	
4740.17	[Ar IV]	8.3 ± 0.2	4.8 ± 0.2	4.9 ± 0.2	8.6 ± 0.2	8.9 ± 0.2	8.9 ± 0.2	-	-	-	3.5 ± 0.7	4.3 ± 0.5	
4861.33	H I	100	100	100	100	100	100	100	100	100	100	100	
4958.91	[O III]	506 ± 1	515 ± 1	578 ± 1	515 ± 1	579 ± 1	579 ± 1	624 ± 8	595 ± 8	353 ± 11	511 ± 6	610 ± 5	
5006.84	[O III]	1520 ± 10	1570 ± 10	1640 ± 10	1520 ± 10	1670 ± 10	1670 ± 10	1820 ± 20	1780 ± 20	1080 ± 20	1470 ± 10	1800 ± 10	
5200.26	[N I]	0.7 ± 0.1	0.6 ± 0.1	0.8 ± 0.2	0.7 ± 0.1	0.5 ± 0.1	0.5 ± 0.1	-	4.1 ± 1.0	-	7.9 ± 0.7	3.9 ± 0.4	
5411.52	He II	3.6 ± 0.1	1.1 ± 0.1	2.3 ± 0.1	3.9 ± 0.1	3.2 ± 0.1	3.2 ± 0.1	-	1.9 ± 0.6	-	1.6 ± 0.5	2.3 ± 0.3	
5517.66	[Cl III]	0.56 ± 0.08	0.74 ± 0.08	0.61 ± 0.09	0.55 ± 0.09	0.75 ± 0.09	0.75 ± 0.09	-	-	-	-	1.19 ± 0.29	
5537.60	[Cl III]	0.81 ± 0.09	0.85 ± 0.09	0.89 ± 0.09	0.81 ± 0.11	1.04 ± 0.09	1.04 ± 0.09	-	-	-	-	0.97 ± 0.25	
5754.60	[N II]	1.8 ± 0.1	1.8 ± 0.1	2.0 ± 0.1	1.6 ± 0.1	1.3 ± 0.1	1.3 ± 0.1	1.8 ± 0.7	4.2 ± 0.9	3.5 ± 1.6	5.3 ± 0.7	3.9 ± 0.4	
5812.14	C IV	0.29 ± 0.09	-	-	0.13 ± 0.09	-	-	-	-	-	-	-	
5875.66	He I	10.5 ± 0.2	11.8 ± 0.2	13.2 ± 0.2	10.4 ± 0.2	11.7 ± 0.2	11.7 ± 0.2	13.0 ± 1.7	10.2 ± 1.3	13.5 ± 2.7	15.3 ± 0.9	13.1 ± 0.6	
6300.30	[O I]	5.6 ± 0.1	4.6 ± 0.2	6.4 ± 0.2	4.7 ± 0.2	3.4 ± 0.1	3.4 ± 0.1	8.5 ± 1.5	14.5 ± 1.7	18.1 ± 2.1	33.5 ± 1.8	20.9 ± 0.9	
6312.10	[S III]	2.3 ± 0.1	2.1 ± 0.1	2.7 ± 0.1	2.4 ± 0.1	2.3 ± 0.1	2.3 ± 0.1	-	1.4 ± 0.5	5.4 ± 1.8	2.7 ± 0.5	2.4 ± 0.3	
6363.77	[O I]	1.93 ± 0.09	1.52 ± 0.09	2.20 ± 0.11	1.58 ± 0.09	1.16 ± 0.10	1.16 ± 0.10	-	5.0 ± 0.9	-	11.4 ± 0.9	6.94 ± 0.55	
6434.73	[Ar V]	1.27 ± 0.08	-	0.41 ± 0.07	1.20 ± 0.09	0.44 ± 0.07	0.44 ± 0.07	-	-	-	-	-	
6548.10	[N II]	26.3 ± 0.2	29.0 ± 0.3	30.9 ± 0.3	23.8 ± 0.3	20.8 ± 0.3	20.8 ± 0.3	42.7 ± 2.8	63.8 ± 3.1	71.1 ± 6.1	95.9 ± 4.8	64.3 ± 1.5	
6562.77	H I	284 ± 1	277 ± 1	277 ± 1	280 ± 1	281 ± 1	281 ± 1	280 ± 9	282 ± 8	273 ± 13	274 ± 10	281 ± 4	
6583.50	[N II]	84.1 ± 0.5	87.4 ± 0.6	89.5 ± 0.6	69.9 ± 0.6	60.3 ± 0.5	60.3 ± 0.5	131.0 ± 5.0	198.0 ± 8.0	214.0 ± 13.0	274.0 ± 13.0	191.0 ± 3.0	
6678.16	He I	2.9 ± 0.1	3.1 ± 0.1	3.3 ± 0.1	2.8 ± 0.1	3.3 ± 0.1	3.3 ± 0.1	3.5 ± 0.9	3.6 ± 0.9	3.9 ± 1.9	4.1 ± 0.6	3.3 ± 0.4	
6716.44	[S III]	2.8 ± 0.1	3.7 ± 0.1	3.8 ± 0.1	2.3 ± 0.1	2.5 ± 0.1	2.5 ± 0.1	6.3 ± 1.0	8.2 ± 1.1	11.4 ± 1.9	22.5 ± 1.6	10.5 ± 0.5	
6730.82	[S III]	5.0 ± 0.1	6.7 ± 0.2	6.9 ± 0.2	4.2 ± 0.1	4.6 ± 0.1	4.6 ± 0.1	8.2 ± 1.0	11.2 ± 1.3	15.5 ± 1.9	27.3 ± 1.7	13.9 ± 0.5	
$\log F(H\beta)$		-10.91	-12.14	-12.25	-11.04	-12.25	-12.25	-13.86	-13.46	-14.11	-14.28	-13.75	
$c(H\beta)$		0.29 ± 0.01	0.29 ± 0.01	0.30 ± 0.01	0.28 ± 0.01	0.25 ± 0.01	0.25 ± 0.01	0.30 ± 0.05	0.25 ± 0.04	0.28 ± 0.08	0.33 ± 0.05	0.27 ± 0.02	
		Electron densities (cm^{-3}) and temperatures (K)											
N _e [S III]		5070 ± 220	5720 ± 250	5450 ± 220	5380 ± 310	5710 ± 290	5710 ± 290	1620 ± 324	2030 ± 360	1920 ± 397	1340 ± 127	1860 ± 111	
N _e [Cl III]		5590 ± 1028	3060 ± 460	5600 ± 980	5780 ± 1210	4810 ± 800	4810 ± 800	-	-	-	-	702 ± 249	
N _e [Ar IV]		4300 ± 77	3670 ± 219	3790 ± 223	4140 ± 141	3780 ± 123	3780 ± 123	-	-	-	2300 ± 633	-	
T _e [N II]		11100 ± 530	10700 ± 620	11300 ± 520	11200 ± 820	11000 ± 980	11000 ± 980	9430 ± 3675	11300 ± 2675	10000 ± 4660	10900 ± 1520	11100 ± 1380	
T _e [O III]		12700 ± 170	12100 ± 220	12000 ± 250	12700 ± 210	12700 ± 240	12700 ± 240	12500 ± 1600	12600 ± 1550	16300 ± 3800	12400 ± 890	12700 ± 600	

Table A8: Ionic and total abundances of NGC 3918.

Abundances	PA=30			PA=70			PA=40			PA=42		
	Neb	Rim	Rim1	Neb	Rim2	B'	B	B''	A'	A	5px-2''	
$10^7 \times \text{He}^+/\text{H}$	6.4 ± 0.1	7.6 ± 0.2	7.8 ± 0.2	6.1 ± 0.2	7.1 ± 0.2	8.5 ± 1.1	8.7 ± 1.0	7.9 ± 1.7	9.9 ± 1.4	8.9 ± 0.7		
$10^2 \times \text{He}^{2+}/\text{H}$	4.02 ± 0.03	1.66 ± 0.02	2.13 ± 0.03	4.19 ± 0.03	3.91 ± 0.03	0.90 ± 0.20	1.90 ± 0.20	2.50 ± 0.40	1.30 ± 0.10	2.46 ± 0.07		
$10^2 \times \text{He}/\text{H}$	10.4 ± 0.1	9.3 ± 0.2	9.9 ± 0.2	10.3 ± 0.2	11.0 ± 0.2	9.4 ± 1.1	10.6 ± 1.0	10.3 ± 1.7	11.3 ± 1.3	11.3 ± 0.7		
$10^3 \times \text{N}^+/\text{H}$	1.4 ± 0.1	1.6 ± 0.1	1.4 ± 0.1	1.1 ± 0.1	1.0 ± 0.1	3.1 ± 2.1	3.0 ± 1.0	4.3 ± 1.5	4.6 ± 0.7	3.1 ± 0.4		
icf(N)	9.7 ± 1.2	8.0 ± 1.2	10.7 ± 1.3	10.7 ± 1.8	11.3 ± 1.9	5.7 ± 2.7	6.9 ± 2.4	3.4 ± 1.5	3.4 ± 0.6	5.6 ± 0.9		
$10^5 \times \text{N}/\text{H}$	13.2 ± 0.9	12.4 ± 1.0	15.3 ± 1.1	12.0 ± 1.1	11.6 ± 1.1	18.3 ± 3.8	20.8 ± 3.9	16.4 ± 3.9	15.7 ± 1.6	17.0 ± 1.3		
$10^6 \times \text{O}^0/\text{H}$	7.2 ± 0.6	6.5 ± 0.7	7.8 ± 0.7	5.7 ± 0.8	4.5 ± 0.7	18.6 ± 7.7	17.2 ± 5.1	31.3 ± 13.9	45.0 ± 8.2	26.2 ± 5.1		
$10^3 \times \text{O}^+/\text{H}$	3.3 ± 0.5	4.4 ± 0.6	3.4 ± 0.5	3.0 ± 0.7	2.9 ± 0.7	7.3 ± 3.5	5.3 ± 1.9	4.2 ± 2.2	11.6 ± 3.0	6.9 ± 1.6		
$10^4 \times \text{O}^{2+}/\text{H}$	2.48 ± 0.04	2.94 ± 0.06	3.18 ± 0.08	2.50 ± 0.05	2.75 ± 0.06	3.14 ± 0.48	2.95 ± 0.41	0.93 ± 0.33	2.61 ± 0.23	2.98 ± 0.16		
icf(O)	1.37 ± 0.01	1.12 ± 0.01	1.15 ± 0.01	1.39 ± 0.01	1.32 ± 0.01	1.06 ± 0.01	1.12 ± 0.02	1.18 ± 0.07	1.07 ± 0.01	1.16 ± 0.01		
$10^4 \times \text{O}/\text{H}$	3.8 ± 0.1	3.8 ± 0.1	4.1 ± 0.1	3.9 ± 0.1	4.0 ± 0.1	4.2 ± 0.6	4.0 ± 0.7	1.7 ± 0.5	4.1 ± 0.4	4.2 ± 0.3		
$10^5 \times \text{Ne}^{2+}/\text{H}$	5.4 ± 0.1	6.5 ± 0.2	7.8 ± 0.2	5.4 ± 0.1	5.6 ± 1.5	8.3 ± 1.5	7.1 ± 1.2	1.2 ± 0.6	8.0 ± 0.9	7.3 ± 0.5		
icf(Ne)	1.37 ± 0.01	1.12 ± 0.01	1.15 ± 0.01	1.40 ± 0.01	1.32 ± 0.01	1.06 ± 0.01	1.12 ± 0.02	1.18 ± 0.07	1.08 ± 0.01	1.16 ± 0.01		
$10^3 \times \text{Ne}/\text{H}$	7.4 ± 0.2	7.2 ± 0.2	9.0 ± 0.3	7.6 ± 0.2	7.4 ± 0.2	8.8 ± 1.6	8.0 ± 1.3	1.4 ± 0.7	8.6 ± 0.9	8.4 ± 0.6		
$10^6 \times \text{Ar}^{3+}/\text{H}$	1.12 ± 0.03	0.77 ± 0.02	0.79 ± 0.03	1.18 ± 0.04	1.23 ± 0.04	0.67 ± 0.22	0.83 ± 0.23	0.38 ± 0.24	0.53 ± 0.09	0.67 ± 0.06		
$10^7 \times \text{Ar}^{4+}/\text{H}$	3.07 ± 0.20	-	1.13 ± 0.19	2.92 ± 0.23	1.07 ± 0.16	-	-	-	-	-		
icf(Ar) ⁽¹¹⁾	1.00 ± 0.00	1.29 ± 0.35	1.00 ± 0.00	1.00 ± 0.00	1.00 ± 0.00	1.29 ± 0.32	1.33 ± 0.14	1.67 ± 0.31	1.52 ± 0.13	1.42 ± 0.07		
$10^6 \times \text{Ar}/\text{H}$	1.43 ± 0.04	0.99 ± 0.40	0.91 ± 0.04	1.48 ± 0.05	1.34 ± 0.04	0.89 ± 0.27	1.12 ± 0.33	0.71 ± 0.45	0.82 ± 0.15	0.96 ± 0.09		
$10^7 \times \text{S}^+/\text{H}$	2.3 ± 0.3	3.5 ± 0.4	3.2 ± 0.3	1.9 ± 0.3	2.3 ± 0.4	4.8 ± 3.2	4.3 ± 1.7	7.9 ± 2.8	10.9 ± 1.7	5.4 ± 0.8		
$10^6 \times \text{S}^{2+}/\text{H}$	2.2 ± 0.1	2.4 ± 0.2	3.2 ± 0.2	2.3 ± 0.1	2.2 ± 0.1	1.3 ± 0.6	1.4 ± 0.6	2.3 ± 0.9	2.8 ± 0.6	2.3 ± 0.4		
icf(S) ⁽¹¹⁾	1.6 ± 0.2	1.5 ± 0.2	1.6 ± 0.2	1.7 ± 0.4	1.7 ± 0.4	1.3 ± 0.7	1.4 ± 0.6	1.2 ± 0.7	1.2 ± 0.3	1.3 ± 0.3		
$10^6 \times \text{S}/\text{H}$	3.9 ± 0.5	4.1 ± 0.5	5.6 ± 0.7	4.2 ± 1.0	4.1 ± 1.0	2.3 ± 1.2	2.6 ± 1.1	3.7 ± 2.2	4.7 ± 1.2	3.7 ± 0.9		
$10^8 \times \text{Cl}^{2+}/\text{H}$	4.8 ± 0.5	6.1 ± 0.5	6.1 ± 0.5	4.9 ± 0.6	6.2 ± 0.5	-	-	-	-	6.9 ± 1.3		
icf(Cl)	2.19 ± 0.06	1.76 ± 0.05	1.92 ± 0.05	2.28 ± 0.09	2.19 ± 0.09	1.00 ± 0.00	1.00 ± 0.00	1.00 ± 0.00	1.00 ± 0.00	1.69 ± 0.06		
$10^8 \times \text{Cl}/\text{H}$	10.5 ± 1.1	10.7 ± 1.0	11.6 ± 1.1	11.0 ± 1.4	13.7 ± 1.1	-	-	-	-	11.6 ± 2.2		

⁽¹¹⁾ Calculated using Kingsburgh & Barlow (1994). When no S⁺² is present, it was calculated using S⁺² = S⁺⁺ [4.677 + (O⁺²/O⁺)^{0.433}] from the same work.

Table A9: NGC 6543

Line	Ion	PA=5					PA=163(12)									
		J	D	A	5px-3.5"	33px-23.1"	Neb	D'	J'	A'	5px-3.5"	33px-23.1"	Neb	A'	5px-3.5"	D'
3727.00	[O III]	103 ± 19	79 ± 2	24 ± 1	22.4±0.6	38±1	106±17	39±1	14±1	22±1	40.3±0.6	22±1	23±1	45.9±0.4	31±1	5px-3.5"
3868.75	[Ne III]	67.6 ± 11.8	52.1±1.0	47.4 ± 0.5	50.1±0.5	55.1±0.9	72.6±8.6	50.2±0.9	47.6±0.4	40.3±0.6	15.9±0.2	16.3±0.4	16.2±0.2	18.8±0.6	18.5±0.6	44.2±1.2
3889.05	H I+He I	25.8 ± 8.1	20.4±0.7	18.2 ± 0.3	19.3±0.3	20.5±0.5	28.3±9.6	16.7±0.4	15.9±0.2	16.3±0.4	13.8±0.6	13.1±0.3	13.1±0.3	12.5±0.8	12.5±0.8	12.5±0.8
3967.46	[Ne III]	26.3±9.9	13.8±0.8	14.4 ± 0.4	16.3±0.4	17.1±0.7	28.8±8.2	15.1±0.4	13.6±0.3	13.8±0.6	15.8±0.6	15.8±0.6	15.8±0.6	15.8±0.6	15.8±0.6	15.8±0.6
3970.07	H I	16.5±9.8	18.0±0.8	16.0±0.4	15.8±0.4	17.6±0.7	16.7±7.8	16.7±0.4	16.3±0.6	16.3±0.6	26.2±0.3	26.2±0.3	26.2±0.3	26.2±0.3	26.2±0.3	26.2±0.3
4101.74	H I	27.8±8.7	23.7±0.6	25.1 ± 0.3	28.8±0.6	27.1±0.3	29.4±7.1	26.3±0.3	26.3±0.3	26.3±0.3	45.8±0.5	45.8±0.5	45.8±0.5	44.7±0.8	44.7±0.8	44.7±0.8
4340.47	H I	55.5±8.6	46.5±0.5	45.2 ± 0.3	46.4±0.3	49.2±0.5	51.8±7.3	46.2±0.3	46.2±0.3	46.2±0.3	2.0±0.1	2.0±0.1	2.0±0.1	1.9±0.1	1.9±0.1	1.9±0.1
4363.21	[O III]	8.0±4.9	2.1±0.2	2.1 ± 0.1	2.3±0.1	2.3±0.2	4.7±3.4	2.3±0.1	2.3±0.1	2.3±0.1	6.3±4.2	6.3±4.2	6.3±4.2	5.8±0.3	5.8±0.3	5.8±0.3
4471.50	He I	7.8±6.3	5.8±0.3	6.0 ± 0.2	6.1±0.2	6.4±0.3	-	6.9±0.2	5.8±0.3	5.8±0.3	6.1±0.4	6.1±0.4	6.1±0.4	6.1±0.4	6.1±0.4	6.1±0.4
4685.68	He II	-	-	-	-	7.7±0.4	-	-	-	-	-	-	-	-	-	-
4711.37	[Ar IV]	-	0.4±0.2	0.8 ± 0.2	1.0±0.1	0.8±0.3	-	0.3±0.1	0.3±0.1	0.3±0.1	0.8±0.1	0.8±0.1	0.8±0.1	0.6±0.1	0.6±0.1	0.3±0.2
4713.17	He I	-	0.8 ± 0.2	0.9 ± 0.2	0.9±0.1	0.9±0.3	-	0.8±0.1	0.8±0.1	0.8±0.1	1.1±0.1	1.1±0.1	1.1±0.1	0.8±0.1	0.8±0.1	0.9±0.2
4740.17	[Ar IV]	-	0.5 ± 0.2	1.1 ± 0.1	1.2±0.1	1.4±0.2	-	0.4±0.1	0.4±0.1	0.4±0.1	1.1±0.1	1.1±0.1	1.1±0.1	0.8±0.1	0.8±0.1	0.5±0.2
4861.33	H I	100	100	100	100	100	100	100	100	100	100	100	100	100	100	100
4958.91	[O III]	242 ± 19	209 ± 5	233 ± 3	229±1	234±1	260±12	229±1	229±1	229±1	216±1	216±1	216±1	223±1	223±1	234±2
5006.84	[O III]	724 ± 62	613 ± 8	691 ± 4	703±4	697±6	775±70	685±1	685±1	685±1	649±1	649±1	649±1	669±1	669±1	702±2
5517.66	[Cl III]	-	0.62 ± 0.11	0.49±0.05	0.51±0.06	0.43±0.11	-	0.61±0.07	0.61±0.07	0.61±0.07	0.39±0.03	0.39±0.03	0.39±0.03	0.43±0.05	0.43±0.05	0.66±0.14
5537.60	[Cl III]	-	0.81 ± 0.10	0.69±0.07	0.71±0.06	0.59±0.13	-	0.93±0.08	0.93±0.08	0.93±0.08	0.72±0.06	0.72±0.06	0.72±0.06	0.64±0.06	0.64±0.06	0.89±0.14
5754.60	[N II]	1.31±0.58	1.23 ± 0.10	0.49 ± 0.06	0.38±0.05	0.65±0.10	1.77±1.66	1.08±0.06	0.26±0.04	0.26±0.04	17.8±0.3	17.8±0.3	17.8±0.3	17.2±0.1	17.2±0.1	19.6±0.3
5875.66	He I	15.5±2.5	14.2±0.2	18.0 ± 0.1	18.0±0.2	16.4±0.2	18.0±2.2	17.8±0.3	16.4±0.1	16.4±0.1	17.8±0.2	17.8±0.2	17.8±0.2	17.2±0.1	17.2±0.1	19.6±0.3
6300.30	[O I]	7.30±1.84	2.44±0.11	0.40 ± 0.04	0.23±0.04	0.93±0.08	6.41±1.57	2.04±0.06	0.06±0.03	0.06±0.03	0.50±0.06	0.50±0.06	0.50±0.06	0.12±0.09	0.12±0.09	0.12±0.09
6312.10	[S III]	-	1.14±0.07	1.24 ± 0.07	1.16±0.07	1.21±0.08	1.38±1.08	1.48±0.06	0.87±0.04	0.87±0.04	1.05±0.09	1.05±0.09	1.05±0.09	1.11±0.05	1.11±0.05	0.92±0.11
6363.77	[O I]	2.68±1.65	0.93±0.08	0.13 ± 0.06	0.06±0.03	0.34±0.09	1.84±1.42	0.70±0.04	0.07±0.02	0.07±0.02	10.9±0.2	10.9±0.2	10.9±0.2	10.0±0.1	10.0±0.1	10.7±0.3
6548.10	[N II]	51.0 ± 5.1	27.6±0.4	9.8 ± 0.3	7.2±0.1	13.5±0.2	31.0±3.8	26.5±0.5	4.1±0.1	4.1±0.1	10.9±0.2	10.9±0.2	10.9±0.2	10.0±0.1	10.0±0.1	10.7±0.3
6562.77	H I	273 ± 15	286 ± 2	281 ± 3	280±2	296±1	277±19	-	-	-	-	-	-	-	-	-
6583.50	[N II]	138.0 ± 11.0	75.9±0.6	25.9 ± 0.2	19.6±0.2	35.5±0.3	97.2±8.0	73.8±1.4	11.8±0.1	11.8±0.1	27.9±0.3	27.9±0.3	27.9±0.3	29.2±0.2	29.2±0.2	27.4±0.4
6678.16	He I	3.95±2.51	3.88±0.15	4.67 ± 0.05	4.05±0.11	4.13±0.11	4.88±2.91	4.41±0.06	4.52±0.09	4.52±0.09	4.52±0.09	4.52±0.09	4.52±0.09	4.52±0.09	4.52±0.09	4.37±0.17
6716.44	[S II]	12.30±2.30	4.33±0.12	1.34 ± 0.08	1.44±0.05	1.78±0.07	14.4±2.4	4.59±0.11	0.65±0.02	0.65±0.02	1.36±0.04	1.36±0.04	1.36±0.04	1.67±0.13	1.67±0.13	1.67±0.13
6730.82	[S II]	13.90±2.40	7.49±0.19	2.44 ± 0.06	1.89±0.05	3.31±0.09	15.4±2.4	7.99±0.18	1.20±0.03	1.20±0.03	2.56±0.09	2.56±0.09	2.56±0.09	2.56±0.06	2.56±0.06	2.96±0.15
<i>log F(Hβ)</i>		-13.16	-11.74	-11.28	-11.25	-10.57	-13.07	-11.27	-11.08	-11.08	-10.49	-10.49	-11.15	-11.15	-11.89	-11.89
<i>e(Hβ)</i>		0.09 ± 0.08	0.26 ± 0.01	0.03 ± 0.01	0.02 ± 0.02	0.22 ± 0.01	0.08±0.08	0.11±0.03	0.03±0.01	0.03±0.01	0.06±0.01	0.06±0.01	0.20±0.03	0.20±0.03	0.14±0.08	0.14±0.08

Table A10: Ionic and total abundances of NGC 6543.

Abundances	PA=5					PA=163(13)						
	J	D	A	Neb	A'	D'	J'	A'	Neb	A'	D'	
$10^2 \times \text{He}^+/ \text{H}$	11.5 ± 2.8	9.8 ± 0.2	11.8 ± 0.1	11.1±0.2	11.9±0.01	12.3±0.2	12.4±2.4	11.7±0.2	10.9±0.1	11.6±0.2	11.2±0.1	12.2±0.2
$10^2 \times \text{He}^{2+}/ \text{H}$	-	-	-	0.60±0.03	-	-	-	-	-	0.48±0.03	-	-
$10^2 \times \text{He}^+ / \text{He}^{2+}$	11.5 ± 2.8	9.8 ± 0.2	11.8 ± 0.1	11.7±0.2	11.9±0.01	12.3±0.2	12.4±2.4	11.7±0.2	10.9±0.1	12.1±0.2	11.2±0.1	12.2±0.2
$10^2 \times \text{N}^+ / \text{H}$	4.81 ± 1.62	1.73 ± 0.16	0.55 ± 0.07	0.77±0.11	0.39±0.06	2.69±0.12	1.50±0.73	1.86±0.10	0.20±0.01	0.75±0.20	0.69±0.08	0.60±0.17
te(N)	5.7 ± 3.4	33.7 ± 7.3	77.6 ± 28.9	22.5±6.0	78.0±19.8	10.9±1.2	32.2±10.2	18.6±8.7	76.6±28.5	32.4±16.1	48.2±11.0	33.1±17.0

Continued on next page

(12) In this PA the [O III]λ5007 Å emission line was saturated, then it was estimated using the theoretical line ratio ([5007]/[4959])=3.01±0.23 from [Acker et al. \(1989\)](#).

$10^5 \times N/H$	28.0 ± 11.6	58.3 ± 8.8	41.3 ± 10.3	17.5 ± 2.7	30.2 ± 4.9	29.1 ± 2.3	54.8 ± 28.0	34.6 ± 2.7	15.6 ± 2.5	23.7 ± 7.4	33.4 ± 3.9	19.7 ± 5.8
$10^6 \times O^0/H$	26.6 ± 12.2	5.0 ± 0.6	0.7 ± 0.2	1.7 ± 0.5	0.3 ± 0.1	8.3 ± 0.5	7.4 ± 4.6	4.6 ± 0.4	0.2 ± 0.1	1.1 ± 0.9	0.9 ± 0.2	0.2 ± 0.1
$10^5 \times O^+/H$	10.3 ± 5.2	5.3 ± 0.9	1.4 ± 0.4	2.5 ± 0.9	1.3 ± 0.4	5.0 ± 0.4	2.9 ± 1.9	3.1 ± 0.3	0.6 ± 0.2	2.1 ± 0.9	1.9 ± 0.4	1.9 ± 0.6
$10^4 \times O^{2+}/H$	1.4 ± 0.6	4.2 ± 0.5	5.1 ± 0.3	4.8 ± 0.5	4.8 ± 0.2	4.9 ± 0.3	2.6 ± 1.2	5.5 ± 0.3	4.7 ± 0.2	5.4 ± 0.6	5.3 ± 0.2	6.2 ± 1.1
icf(O)	1.00 ± 0.00	1.00 ± 0.00	1.00 ± 0.00	1.03 ± 0.01	1.00 ± 0.00	1.00 ± 0.00	1.00 ± 0.00	1.00 ± 0.00	1.00 ± 0.01	1.02 ± 0.01	1.00 ± 0.01	1.00 ± 0.00
$10^4 \times O/H$	2.9 ± 1.2	4.7 ± 0.5	5.3 ± 0.3	5.2 ± 0.6	4.9 ± 0.2	5.5 ± 0.3	3.2 ± 1.4	5.8 ± 0.3	4.8 ± 0.2	5.8 ± 0.7	5.5 ± 0.2	6.4 ± 1.2
$10^5 \times Ne^{2+}/H$	3.9 ± 1.8	12.6 ± 1.2	13.1 ± 0.8	13.9 ± 1.8	12.8 ± 0.7	15.2 ± 1.1	8.3 ± 4.0	15.0 ± 0.9	12.7 ± 0.6	14.2 ± 1.8	13.5 ± 0.8	14.6 ± 2.4
icf(Ne)	3.54 ± 1.44	1.76 ± 0.09	1.39 ± 0.03	1.03 ± 0.01	1.11 ± 0.07	1.67 ± 0.04	1.77 ± 0.69	1.50 ± 0.02	1.10 ± 0.01	1.03 ± 0.01	1.13 ± 0.01	1.40 ± 0.08
$10^7 \times Ne^{3+}/H$	16.3 ± 7.5	22.3 ± 2.2	18.2 ± 1.1	14.3 ± 1.9	14.3 ± 0.7	25.5 ± 1.6	16.4 ± 8.3	22.6 ± 1.2	13.9 ± 0.8	14.6 ± 1.8	15.2 ± 0.8	20.7 ± 4.6
$10^7 \times Ar^{3+}/H$	-	2.7 ± 0.8	6.4 ± 0.7	5.7 ± 1.2	6.6 ± 0.5	2.0 ± 0.5	-	3.2 ± 0.4	6.3 ± 0.4	7.0 ± 1.4	4.7 ± 0.4	3.1 ± 1.1
icf(Ar) ⁽¹⁴⁾	1.00 ± 0.00	1.11 ± 0.24	1.03 ± 0.01	1.09 ± 0.02	1.03 ± 0.01	1.09 ± 0.01	1.00 ± 0.00	1.05 ± 0.01	1.01 ± 0.01	1.07 ± 0.05	1.04 ± 0.01	1.03 ± 0.02
$10^7 \times Ar/H$	-	3.0 ± 0.9	6.6 ± 0.7	6.2 ± 1.1	6.8 ± 0.5	2.2 ± 0.5	-	3.4 ± 0.4	6.3 ± 0.4	7.6 ± 1.6	4.9 ± 0.4	3.3 ± 1.3
$10^7 \times S^7/H$	11.0 ± 3.8	4.4 ± 0.4	1.4 ± 0.2	2.0 ± 0.5	1.0 ± 0.2	6.7 ± 0.4	6.0 ± 2.8	5.2 ± 0.3	0.6 ± 0.1	1.9 ± 0.9	1.7 ± 0.2	1.7 ± 0.6
$10^6 \times S^{4+}/H$	6.4 ± 4.2	6.8 ± 0.8	8.3 ± 0.7	7.2 ± 0.9	7.0 ± 0.6	14.0 ± 0.9	3.0 ± 2.5	10.8 ± 0.8	5.7 ± 0.4	7.6 ± 1.1	8.1 ± 0.5	7.5 ± 1.5
icf(S) ⁽¹⁴⁾	1.1 ± 0.7	1.5 ± 0.3	2.3 ± 0.7	1.9 ± 0.7	2.3 ± 0.7	1.6 ± 0.2	1.6 ± 1.3	1.9 ± 0.2	3.0 ± 1.0	2.1 ± 0.9	2.2 ± 0.5	2.3 ± 0.8
$10^6 \times S/H$	8.2 ± 5.2	10.9 ± 2.2	19.4 ± 5.9	14.1 ± 5.2	16.3 ± 5.0	23.5 ± 2.9	5.8 ± 4.7	21.5 ± 2.3	17.3 ± 5.8	16.4 ± 7.0	18.2 ± 4.1	17.6 ± 6.1
$10^8 \times Cl^{2+}/H$	-	17.9 ± 2.8	16.0 ± 1.7	12.9 ± 2.7	14.9 ± 1.3	19.3 ± 4.3	-	17.9 ± 2.6	12.4 ± 1.0	14.9 ± 3.7	15.3 ± 1.5	25.0 ± 12.9
icf(Cl)	1.00 ± 0.00	1.62 ± 0.06	1.00 ± 0.00	1.00 ± 0.09	1.00 ± 0.00	1.69 ± 0.04	1.00 ± 0.00	1.88 ± 0.04	1.00 ± 0.00	1.00 ± 0.81	1.00 ± 0.00	1.00 ± 0.00
$10^8 \times Cl/H$	-	29.1 ± 4.9	16.0 ± 1.7	17.7 ± 5.8	14.9 ± 1.3	32.5 ± 7.6	-	32.0 ± 4.8	12.4 ± 1.0	17.7 ± 5.3	15.3 ± 1.7	25.0 ± 12.9

⁽¹³⁾ In this PA, abundance estimation may not be reliable.

⁽¹⁴⁾ Calculated using Kingsburgh & Barlow (1994). When no S^{+2} is present, it was calculated using $S^{+2} = S^{+1} [4.677 + (O^{+2}/O^{+1})^{0.433}]$ from the same work.

Table A11: NGC 6905.

Line	Ion	PA=161					
		South Rim 6px-4.2"	Neb 60px-42"	North Rim 8px-5.6"	NW knot2 6px-4.2"	NW knot 8px-5.6"	
3727.00	[O III]	11.6±2.5	19.6±3.8	30.0±3.1	54.4±8.3	214±27	
3868.75	[Ne III]	71.5±3.2	94.9±3.2	102.0±3.0	112.0±7.0	134.0±14.0	
3889.05	H I+He I	12.3±1.5	29.3±3.2	14.7±1.3	16.2±3.6	21.2±6.8	
3967.46	[Ne III]	23.0±2.0	23.1±3.3	33.4±2.4	38.7±5.1	41.3±8.3	
3970.07	H I	16.0±1.9	15.8±3.4	15.9±2.4	16.2±5.1	16.9±8.2	
4101.74	H I	28.5±1.6	27.4±1.9	26.9±0.9	28.9±4.4	29.7±8.7	
4340.47	H I	50.8±1.5	49.6±1.7	48.1±1.9	53.2±3.5	51.9±8.5	
4363.21	[O III]	11.7±0.7	11.9±1.2	13.8±0.9	18.7±2.4	26.9±7.6	
4471.50	He I	1.0±0.3	1.1±0.1	-	-	-	
4685.68	He II	105.0±2.0	105.0±2.0 (15)	90.1±2.0	97.7±4.1	53.7±6.6	
4711.37	[Ar IV]	8.0±0.6	15.8±1.2	5.9±0.9	7.8±1.5	-	
4713.17	He I	0.14±0.06	0.17±0.05	-	-	-	
4740.17	[Ar IV]	6.0±0.5	13.5±0.8	4.1±0.6	5.8±1.5	-	
4861.33	H I	100	100	100	100	100	
4958.91	[O III]	255±1	311±3	377±3	372±3	346±5	
5006.84	[O III]	767±1	934±5	1150±10	1120±10	1070±10	
5411.52	He II	9.9±0.5	15.5±1.2	7.9±0.7	6.6±1.2	-	
5517.66	[Cl III]	0.8±0.2	1.1±0.6	-	-	-	
5537.60	[Cl III]	0.6±0.2	1.0±0.6	-	-	-	
5754.60	[N III]	-	-	-	-	-	
5875.66	He I	3.2±0.3	6.4±0.7	4.0±0.4	5.8±0.9	7.0±1.8	
6300.30	[O I]	1.5±0.2	1.5±0.4	-	7.7±1.1	30.9±3.5	
6312.10	[S III]	1.6±0.2	2.7±0.5	2.8±0.3	2.6±0.9	-	
6363.78	[O I]	0.8±0.2	0.5±0.3	-	2.0±0.7	12.1 ±2.3	
6548.10	[N II]	2.7±0.3	4.8±0.4	5.2±0.3	9.6±1.0	42.2±4.3	
6562.77	H I	282±4	281±3	281±4	279±8	272 ±15	
6583.50	[N II]	7.2±0.4	14.1±0.4	13.4±0.6	24.4±1.6	122.0±9.0	
6678.16	He I	1.81±0.32	1.72±0.35	1.93±0.29	-	-	
6716.44	[S II]	1.70±0.28	2.50±0.36	3.75±0.37	7.74±0.86	16.20±2.20	
6730.82	[S II]	1.49±0.26	2.57±0.36	3.16±0.31	6.51±0.76	13.10±2.10	
log F(H β)		-12.34	-11.33	-12.39	-13.22	-13.38	
c(H β)		0.03±0.02	0.02±0.01	0.03±0.02	0.05±0.04	0.10±0.09	
Electron Densities (cm ⁻³) and Temperatures (K)							
N _e [S II]		346±83	743±149	280±39	291±47	219±46	
N _e [Ar IV]		204±23	1390±134	-	-	-	
N _e [Cl III]		-	661±536	-	-	-	
T _e [O III]		13600±814	12600±1272	12400±813	14100±1812	17100±4833	
Stellar line fluxes from CSPN (erg/cm ²)							
O VI λ 3811			(2.07±0.04)×10 ⁻¹¹			18±1	
O VI λ 3834			(1.12±0.03)×10 ⁻¹¹			24±1	
C IV λ 4658			(5.73±0.08)×10 ⁻¹²			30±1	
O VI λ 5291			(8.36±0.03)×10 ⁻¹³			19±2	
C IV λ 5471			(3.34±0.38)×10 ⁻¹³			22±1	
C IV λ 45801,5812			(2.64±0.08)×10 ⁻¹²			40±1	

(15) According to Gómez-González et al. (2022), this emission is from both central star and nebula.

Table 12: Ionic and total abundances of NGC 6905.

Abundances	PA=161					
	South rim	Neb	North Rim	NW knot2	NW knot	
10 ² × He ⁺ /H	2.6±0.3	3.8±0.4	3.5±0.4	4.0±0.8	5.1±1.5	
10 ² × He ²⁺ /H	9.1±0.2	9.9±0.2	7.7±0.2	8.3±0.3	4.7±0.6	
10 ² × He/H	11.8±0.3	13.7±0.5	11.2±0.4	12.4±0.9	9.8±1.6	
10 ⁶ × N ⁺ /H	0.75±0.06	1.65±0.18	1.72±0.12	2.40±0.30	8.07±1.80	
icf(N)	171±51	93.9±25.2	73.4±10.3	43.3±9.7	9.4±1.7	
10 ⁵ × N/H	12.9±4.0	15.6±4.5	12.6±1.9	10.5±2.7	7.7±1.8	
10 ⁶ × O ⁰ /H	1.2±0.2	1.2±0.4	-	4.4±1.0	11.5±6.4	
10 ⁶ × O ⁺ /H	1.4±0.4	3.3±0.9	5.0±0.8	5.8±1.6	12.9±4.0	
10 ⁴ × O ²⁺ /H	1.1±0.1	1.6±0.2	2.0±0.2	1.4±0.2	0.8±0.4	
icf(O)	3.2±0.3	2.6±0.2	2.4±0.2	2.3±0.4	1.3±0.2	
10 ⁴ × O/H	3.4±0.4	4.2±0.7	4.9±0.5	3.4±0.7	1.5±0.7	
10 ⁵ × Ne ²⁺ /H	2.6±0.3	4.2±0.7	5.1±0.5	3.8±0.7	2.6±0.7	
icf(Ne)	3.6±0.4	2.9±0.3	2.5±0.3	2.4±0.5	1.6±0.3	
10 ⁴ × Ne/H	0.9±0.1	1.2±0.2	1.3±0.2	0.9±0.2	0.4±0.2	
10 ⁷ × Ar ³⁺ /H	8.0±0.8	20.9±3.8	7.3±0.9	7.0±1.7	-	
icf(Ar)(16)	2.74±0.19	2.42±0.15	2.23±0.13	2.18±0.27	1.00±0.00	
10 ⁶ × Ar/H	2.2±0.3	5.0±0.7	1.6±0.2	1.5±0.4	-	
10 ⁸ × S ⁷⁺ /H	3.9±0.6	7.6±1.3	10.0±0.9	16.2±2.4	24.0±8.1	
10 ⁶ × S ²⁺ /H	1.2±0.2	2.6±0.7	2.8±0.4	1.7±0.7	1.6±0.9	
icf(S)(16)	4.3±1.3	3.5±1.1	3.2±0.6	2.7±0.9	1.6±0.9	
10 ⁶ × S/H	5.3±1.6	9.4±2.9	9.3±1.7	5.0±1.7	2.9±1.6	
10 ⁸ × Cl ²⁺ /H	3.5±0.9	7.0±2.9	-	-	-	
icf(Cl)	1.00±0.00	1.00±0.00	1.00±0.00	1.00±0.00	1.00±0.00	
10 ⁸ × Cl/H	3.5±0.9	7.0±2.9	-	-	-	

(16) Calculated using Kingsburgh & Barlow (1994). When no S²⁺ is present, it was calculated using S²⁺ = S⁺[4.677 + (O²⁺/O⁺)^{0.433}] from the same work.

This paper has been typeset from a $\text{\TeX}/\text{\LaTeX}$ file prepared by the author.